

# Nonlinear Characteristics of Tuned Liquid Dampers

by

Jin Kyu Yu

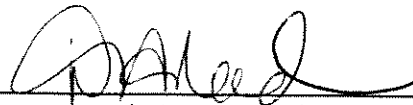
A dissertation submitted in partial  
fulfillment of the requirements for the  
degree of

Doctor of Philosophy

University of Washington

1997

Approved by



Chairperson of Supervisory Committee

---

---

---

---

Program Authorized  
to Offer Degree

---

Date

---

University of Washington

Abstract

Nonlinear Characteristics of Tuned Liquid Dampers

by Jin Kyu Yu

Chairperson of the Supervisory Committee: Professor Dorothy A. Reed  
Department of Civil Engineering

In recent years, tuned liquid dampers (TLD) have been successfully employed in practice to mitigate undesirable structural vibrations. Although this device has many advantages, its damping mechanism has not been thoroughly investigated, nor are any definite guidelines available for TLD design. In this study, the behavior of TLD is investigated experimentally and numerically. The results are incorporated into the development of a design procedure.

Shaking table experiments were conducted to investigate the characteristics of the shallow water sloshing motion in rectangular or circular tanks under small and large amplitude excitations. The results reveal that the most distinguishing characteristic of the shallow-water is a hardening-spring type nonlinearity. The nonlinearity is explicitly quantified using the jump-frequency as a function of excitation amplitude and tank size. It was found that the characteristics of nonlinearity are different in two regions: identified as the weak wave breaking and strong wave breaking regions.

An equivalent TMD model was developed to capture the energy dissipation capacity of the TLD based on the experimental results by means of energy dissipation curve matching. The nonlinear stiffness and damping characteristics of the TLD were incorporated into this model as functions of excitation amplitude and tank size.

A numerical fluid model using the random choice method to solve the shallow-water wave equations proposed by Gardarsson and Yeh (1994) was employed to simulate shallow-water sloshing motion in a rectangular tank. It was found that the model accurately simulated weak or moderate wave breaking. However, the model cannot capture the wave phenomenon under extremely strong excitation motions.

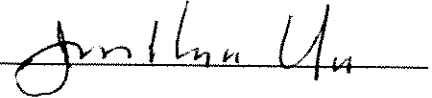
Numerical schemes were developed to simulate the dynamic motions of a single-degree-of-freedom structure coupled with a TLD. Based on the captured nonlinear properties of the TLD, a nonlinear tuning procedure is proposed. The performance of TLDs in mitigating the structural vibration was evaluated using the interaction model of a structure with a proposed equivalent TMD. The results reveal that the nonlinear tuning enhances the TLD performance. A TLD design procedure under harmonic and white noise excitations is developed based on the results of performance investigations.

Finally, the performance of TLDs under wind or earthquake conditions was investigated numerically. For the simulated wind condition, the selected TLD reduced the structural vibrations significantly. For the Northridge earthquake, the TLD was ineffective during the initial stage of the earthquake. The performance of the TLD for earthquake loadings must be further investigated.

## Doctoral Dissertation

In presenting this dissertation in partial fulfillment of the requirements for the Doctoral degree at the University of Washington, I agree that the Library shall make its copies freely available for inspection. I further agree that extensive copying of this dissertation is allowable only for scholarly purposes, consistent with "fair use" as prescribed in the U.S. Copyright Law. Requests for copying or reproduction of this dissertation may be referred to University Microfilms, 1490 Eisenhower Place, P.O. Box 975, Ann Arbor, MI 48106, to whom the author has granted "the right to reproduce and sell (a) copies of the manuscript in microform and/or (b) printed copies of the manuscript made from microform."

Signature



Date

1/29/97

## TABLE OF CONTENTS

|   |    |
|---|----|
| LIST OF FIGURES.....  | iv |
| LIST OF TABLES .....  | ix |
| NOTATION AND ABBREVIATIONS.....   | x  |
| CHAPTER 1. INTRODUCTION.....  | 1  |
| 1.1 Tuned Liquid Damper (TLD).....  | 1  |
| 1.2 Damping Mechanism of the TLD .....  | 3  |
| 1.3 Performance Measurement of Damping Devices.....   | 4  |
| 1.4 Objectives and Scope of Work.....   | 5  |
| CHAPTER 2. EXPERIMENTAL INVESTIGATIONS OF SHALLOW WATER<br>WAVES IN RECTANGULAR AND CIRCULAR TANKS .....          | 8  |
| 2.1 Shaking Table Tests.....  | 8  |
| 2.1.1 Test Set-up.....  | 8  |
| 2.1.2 Test Cases .....  | 10 |
| 2.2 Characteristics of Water Sloshing Motion in Rectangular Tanks.....  | 12 |
| 2.2.1 Time History Responses of Water Sloshing Motion at Steady State for<br>Harmonic Excitation.....             | 14 |
| 2.2.2 Frequency Responses of Water Sloshing Motion.....   | 19 |
| 2.2.3 Higher Modes of Water Sloshing Motion.....  | 27 |
| 2.2.4 Calculation of the Base Shear Force Based on the Wave Height near<br>the End wall of Rectangular Tank ..... | 29 |
| 2.3 Water Sloshing Motion in Circular Tanks.....  | 32 |
| CHAPTER 3. NUMERICAL MODELS OF THE TLD .....  | 35 |
| 3.1 NSD Model - an Empirically-based Equivalent TMD Model .....   | 35 |

|  |     |
|--|-----|
| 3.1.1 Modeling.....  | 35  |
| 3.1.2 Energy Dissipation Matching Scheme .....   | 37  |
| 3.1.3 Determination of the Model Parameters based on Shaking Table Test<br>Results for Rectangular TLDs..... | 39  |
| 3.1.4 Application of the Equivalent TMD Model derived for Rectangular<br>TLDs to the Circular TLD .....      | 42  |
| 3.2 RCM Model - a Numerical Fluid Model .....  | 45  |
| 3.2.1 Shallow-water Wave Theory.....   | 45  |
| 3.2.2 Numerical Simulation of Water Sloshing Motion using the RCM Model ..                                   | 46  |
| CHAPTER 4. DEVELOPMENT OF TLD DESIGN PROCEDURES.....   | 52  |
| 4.1 Interaction of a TLD with a SDOF Structure .....   | 52  |
| 4.1.1 Time History Numerical Solution Schemes .....  | 52  |
| 4.1.2 Evaluation of the NSD Model and the RCM Model .....  | 56  |
| 4.2 TLD Performance and Design Procedure for Harmonic Excitations.....                                       | 64  |
| 4.2.1 Frequency Response Analysis .....  | 64  |
| 4.2.2 TLD Tuning - Linear Tuning and Nonlinear Tuning .....  | 67  |
| 4.2.3 TLD Performance for Harmonic Excitations .....   | 68  |
| 4.2.4 TLD Design Guide for Harmonic Excitations.....   | 73  |
| 4.3 TLD Performance and Design Procedure for White Noise Excitations.....                                    | 77  |
| 4.3.1 Time History Analysis.....   | 77  |
| 4.3.2 Spectral Analysis .....  | 81  |
| 4.3.3 TLD Performance for White Noise Excitations .....  | 83  |
| 4.3.4 TLD Design Guide for White Noise Excitations.....  | 86  |
| 4.4 TLD Performance under Wind Conditions .....  | 88  |
| 4.5 Behavior of the TLD under Earthquake Excitations .....   | 93  |
| 4.5.1 Validity of the NSD Model for the Earthquake Condition .....   | 93  |
| 4.5.2 Performance of the TLD for Earthquake Excitations.....   | 95  |
| CHAPTER 5. CONCLUSIONS.....  | 102 |

|  |     |
|--|-----|
| REFERENCES .....   | 105 |
| Appendix A. Linear SDOF System.....  | 111 |
| A.1 Frequency Response Analysis .....  | 111 |
| A.2 Energy Dissipation per cycle by a SDOF Damping Device .....  | 113 |
| Appendix B. Linear 2DOF System for Harmonic Excitation.....  | 117 |
| B.1 Frequency Response Analysis .....  | 117 |
| B.2 Optimum Design Parameters of the Linear Mechanical Damper .....  | 119 |
| B.3 Performance of the TMD - Case Study .....  | 120 |
| Appendix C. Linear 2DOF System for White Noise Excitations .....   | 124 |
| C.1 Steady-state Responses.....  | 124 |
| C.2 Optimum Design Parameters for the Linear Mechanical Damper.....  | 127 |
| Appendix D. Time History Analysis for a SDOF Structure equipped with a TLD<br>under an Arbitrary Excitation..... | 128 |
| Appendix E. The Results of the Shaking Table Experimental Investigations .....                                   | 130 |
| Appendix F. Shallow-Water Wave Theory.....   | 132 |

## LIST OF FIGURES

| <i>Number</i>   | <i>Page</i> |
|---|-------------|
| Figure 1.1 Mechanisms of the mechanical dampers (TLD & TMD).....  | 3           |
| Figure 2.1 Shaking table experiment set-up.....   | 9           |
| Figure 2.2 Rectangular and circular TLD configurations .....  | 10          |
| Figure 2.3 Sample time histories of water sloshing motion in the shaking table tests for the case of the tank with length $L=590$ mm, water depth $h_0=30$ mm, and excitation amplitude $A=20$ mm; the water surface elevation, $\eta$ , at the end wall and at the mid-tank and the base shear force, $F_w$ , in the direction of along and across excitation..... | 15          |
| Figure 2.4 Sample time histories of the nondimensional wave heights for the steady-state wave motion at various excitation frequencies for the cases of the tank with length $L = 590$ mm, water depth $h_0 = 30$ mm and excitation amplitude $A = 10, 20$ and $40$ mm, respectively. ....  | 17          |
| Figure 2.5 Sample time histories of the measured base shear force in the $x$ -direction for the same conditions as Figure 2.4.....  | 18          |
| Figure 2.6 Energy dissipation curves of the base shear force $F_w$ vs. the shaking table displacement $x_s$ for the same conditions as Figure 2.5. The dashed lines represent calculations including higher modes up to 9th mode; the solid line represents calculations only including the first mode.....   | 20          |
| Figure 2.7 Sample frequency responses of water sloshing motion in shaking table tests of the tank with length $L = 590$ mm, water depth $h_0 = 30$ mm and excitation amplitude $A = 10, 20$ and $40$ mm.....  | 22          |
| Figure 2.8 Sample frequency responses for the selected experimental cases to investigate the effect of water depth $h_0$ on the water sloshing motion.....  | 24          |
| Figure 2.9 Sample frequency responses for the selected experimental cases to investigate the effect of tank length $L$ on the water sloshing motion.....  | 24          |
| Figure 2.10 Relationship between the jump frequency ratio and the nondimensional excitation amplitude based on experimental results.....  | 26          |

|  |    |
|--|----|
| Figure 2.11 The effects of higher frequency components of the water sloshing motion upon its frequency responses for the tank with length $L = 590$ mm, water depth $h_0 = 30$ mm and excitation amplitude $A = 20$ mm.....  | 28 |
| Figure 2.12 Comparison of the base shear force, $F_\eta$ , calculated from the wave height and the one measured by the load cell, $F_w$ , for the tank with length $L=590$ mm, water depth $h_0=30$ mm and excitation amplitude $A=20$ mm.....                                 | 30 |
| Figure 2.13 Sample time history responses of water sloshing motion for the circular tank with diameter $D=690$ mm, water depth $h_0=30$ mm and excitation amplitude $A=20$ mm.....   | 33 |
| Figure 2.14 Sample frequency responses of water sloshing motion for the circular tank with diameter $D=690$ mm, water depth $h_0=30$ mm and excitation amplitude $A=20$ mm.....  | 34 |
| Figure 3.1 An equivalent TMD model of the TLD.....   | 36 |
| Figure 3.2 Matching scheme of the sweep frequency energy dissipation curves to obtain the stiffness hardening ratio, $\kappa$ and damping ratio, $\zeta_d$ of the NSD model of the TLD with length $L=590$ mm, water depth $h_0=30$ mm and excitation amplitude $A=20$ mm..... | 38 |
| Figure 3.3 The damping ratio, $\zeta_d$ and the stiffness hardening ratio, $\kappa$ , of the NSD model of the rectangular TLD determined from shaking table experiment.....  | 41 |
| Figure 3.4 The damping ratio, $\zeta_d$ and the stiffness hardening ratio, $\kappa$ , of the NSD model of the circular TLD determined from shaking table experiment.....   | 44 |
| Figure 3.5 Sample time history responses of water sloshing motion simulated using the RCM model for the rectangular tank with length $L=590$ mm, water depth $h_0=30$ mm and excitation amplitude $A=20$ mm .....  | 48 |
| Figure 3.6 Sample frequency responses of water sloshing motion simulated using the RCM model for the rectangular tank with length $L=590$ mm, water depth $h_0=30$ mm and excitation amplitude $A=20$ mm .....   | 49 |
| Figure 3.7 The damping ratio, $\zeta_d$ , and the stiffness hardening ratio, $\kappa$ , of rectangular TLDs determined from numerical analyses using the RCM model.....  | 50 |
| Figure 4.1 A SDOF structure with a TLD .....   | 53 |

|             |  |    |
|-------------|--|----|
| Figure 4.2  | A numerical solution scheme for the responses of a SDOF structure coupled with a TLD. The TLD is simulated using the RCM model.....  | 54 |
| Figure 4.3  | An arbitrary time history structural displacement.....   | 54 |
| Figure 4.4  | A numerical solution scheme for the responses of a SDOF structure coupled with a TLD. The TLD is characterized as the NSD model.....   | 55 |
| Figure 4.5  | Sample time history responses of the SDOF structure coupled with a TLD. The TLD is characterized as the RCM and the NSD models, respectively. The excitation amplitude is in the region of weak wave breaking.....   | 58 |
| Figure 4.6  | Sample time histories of the NSD model properties for the TLD for the same cases as Figure 4.5. ....   | 59 |
| Figure 4.7  | The maximum displacements of the structure coupled with a TLD at sweep excitation frequencies. The TLD is characterized as the RCM and the NSD models, respectively. The excitation amplitude is in the region of weak wave breaking.....  | 60 |
| Figure 4.8  | Sample time history responses of the SDOF structure coupled with a TLD. The TLD is characterized as the RCM and the NSD models, respectively. The excitation amplitude near resonance falls into the region of strong wave breaking. ....  | 62 |
| Figure 4.9  | Sample time history responses of the SDOF structure coupled with a TLD. The TLD is characterised as the RCM and the NSD models, respectively. The selected system is in the condition beyond the experimental cases. ....  | 63 |
| Figure 4.10 | A SDOF structure equipped with a TLD (NSD model) .....   | 65 |
| Figure 4.11 | A solution procedure for the frequency responses of a structure coupled with a TLD as the structure is subjected to harmonic excitations. The TLD is characterized as the NSD model. ....  | 66 |
| Figure 4.12 | Frequency responses of the structure coupled with various TLDs. The natural frequency and the damping ratio of the structure are $f_s=0.32$ Hz and $\zeta_s=1.0$ % respectively. The mass ratio $\mu=1.0\%$ . The estimated maximum acceleration of the structure with the TLD $x_{0,max}$ is approximately 20 milli-g. .... | 71 |
| Figure 4.13 | Frequency responses of the structure coupled with various TLDs. The natural frequency and the damping ratio of the structure are $f_s=0.32$  |    |

|   |    |
|---|----|
| Hz and $\zeta_s=1.0\%$ respectively. The mass ratio $\mu=1.0\%$ . The estimated maximum acceleration of the structure with the TLD $x_{0,max}$ is approximately 3 milli-g. ....   | 72 |
| Figure 4.14 Maximum structural displacements. Curves are for the structure equipped with linear mechanical dampers with various tuning ratios. Circle-marks are for the structure equipped with linearly tuned liquid dampers. Cross-marks are for the structure equipped with nonlinearly tuned liquid dampers. Damping ratio of the structure, $\zeta_s=1.0\%$ . Mass ratio, $\mu=1.0\%$ . .... | 75 |
| Figure 4.15 A searching scheme for selection of the most effective TLD for a given excitation amplitude.....  | 76 |
| Figure 4.16 Sample plots of a generated white noise random forcing and the structural motion induced by the random forcing.....   | 78 |
| Figure 4.17 Sample time histories for the damping ratio and tuning ratio of the TLD for the system described in Figure 4.16.....  | 73 |
| Figure 4.18 A solution procedure for the stochastic responses of a structure coupled with a TLD as the structure is subjected to white noise excitation. The TLD is treated as the NSD model. ....  | 84 |
| Figure 4.19 The results from sample spectral analyses and time history analyses as compared with a family of curves for the system with a linear TMD system .....   | 87 |
| Figure 4.20 A sample set of the simulated time series for wind pressure using the AR(2) model and the structural displacement with a TLD under this wind pressure loading. The properties of the structure and the TLD are: $f_s = 0.32$ Hz; $\zeta_s = 1.0\%$ ; $\mu = 1.0\%$ ; $L = 171$ cm; $h_0 = 12.4$ cm.....   | 90 |
| Figure 4.21 Time histories of $\zeta_d$ and $\gamma$ of the NSD model for the case of Figure 4.20.....  | 91 |
| Figure 4.22 Ground motions during the El Centro earthquake obtained from "NCEER Strong-Motion Data Base" and scaled total displacements of a undamped structure with natural frequency $f_s = 0.5$ Hz.....  | 94 |
| Figure 4.23 Damping forces and energy dissipation per cycle generated by the TLD with the length $L = 590$ mm, water depth $h_0 = 36$ mm and its corresponding NSD model. The maximum shaking table displacement $x_{s,max}$ was adjusted to approximately 40 mm. ....  | 96 |

|   |     |
|---|-----|
| Figure 4.24 Time histories for $\zeta_d$ and $\kappa$ of the NSD model for the case of Figure 4.23 .....  | 97  |
| Figure 4.25 Time history records of ground motions during the 1994 Northridge earthquake .....  | 98  |
| Figure 4.26 Time history responses of the structure with and without a TLD under the Northridge earthquake. The properties of the structure and the TLD are: $f_s = 0.32$ Hz; $\zeta_s = 1.0$ %; $\mu = 1.0$ %; $L = 171$ cm; $h_0 = 11.6$ cm ..... | 100 |
| Figure 4.27 Time histories for $\zeta_d$ and $\gamma$ of the NSD model for the case of Figure 4.26 .....  | 101 |
| Figure A.1 SDOF system.....   | 111 |
| Figure A.2 Frequency responses of SDOF systems with various damping values.....   | 114 |
| Figure A.3 Energy dissipation curves for SDOF systems with various damping or various stiffness values.....   | 116 |
| Figure B.1 SDOF structure equipped with a damper.....   | 117 |
| Figure B.2 Frequency response of lightly damped structures with variously damped TMDs.....  | 120 |
| Figure B.3 Time history free vibration responses of lightly damped structures with variously damped TMDs under harmonic excitation .....  | 121 |
| Figure B.4 Time history forced vibration responses of lightly damped structures with variously damped TMDs under harmonic excitation .....  | 122 |
| Figure B.5 Time history forced vibration responses of lightly damped structures with variously damped TMDs under harmonic excitation .....  | 123 |
| Figure C.1 SDOF structure equipped with a damper.....   | 124 |
| Figure F.1 Geometry of the shallow water wave .....   | 132 |

## LIST OF TABLES

### *Number Page*

|           |  |     |
|-----------|--|-----|
| Table 2.1 | Data for the experimental investigations of rectangular tanks .....  | 11  |
| Table 2.2 | Data for the experimental investigations of circular tanks.....  | 11  |
| Table 4.1 | Data for case studies - Evaluation of the NSD model and the RCM model.....   | 56  |
| Table 4.2 | Properties and performance of TLDs attached to a structure at resonance.....   | 70  |
| Table 4.3 | Responses of a SDOF structure with various TLDs under white noise excitation obtained from time history analyses. ( $f_s = 0.32$ Hz, $\zeta_s = 1.0$ %, $\mu = 1.0$ %, targeted $\ddot{x}_{s,max} = 20$ milli-g).....            | 80  |
| Table 4.4 | Responses of a SDOF structure with various TLDs under white noise excitation obtained from the proposed stochastic analysis. ( $f_s = 0.32$ Hz, $\zeta_s = 1.0$ %, $\mu = 1.0$ %, targeted $\ddot{x}_{s,max} = 20$ milli-g)..... | 85  |
| Table 4.5 | Responses of a SDOF structure with various TLDs as the structure is subjected to wind. ( $f_s = 0.32$ Hz, $\zeta_s = 1.0$ %, $\mu = 1.0$ %, targeted $\ddot{x}_{s,max} = 20$ milli-g).....                                       | 89  |
| Table E.1 | The data and results for the rectangular tanks.. .....   | 130 |
| Table E.2 | The data for the rectangular TLDs obtained from the numerical simulation using the random choice method.....   | 131 |
| Table E.3 | The data for the circular tanks.. .....  | 131 |

## NOTATION AND ABBREVIATIONS

|            |  |
|------------|--|
| $A$        | Amplitude of base excitation<br>Maximum structural displacement                            |
| $A_{\max}$ | Maximum allowable structural displacement  |
| $B, b$     | Tank width   |
| $D$        | Tank diameter  |
| $E$        | Energy   |
| $E[ \ ]$   | Ensemble average of the quantity in [ ]  |
| $E_d$      | Energy dissipation by the damper   |
| $F$        | Force  |
| $F_w$      | Base shear force due to water sloshing   |
| $F_\eta$   | Hydrodynamic force calculated based on hydrostatic water pressure on the tank end walls.   |
| $H_{a/b}$  | Complex frequency response function relating output $a$ to input $b$ .                     |
| $L$        | Tank length  |
| $S$        | Spectral density function  |
| $S_0$      | Constant spectral density of white noise input   |
| $T$        | Fundamental period   |
| $c$        | Damping coefficient  |
| $c_{cr}$   | Critical damping coefficient ( $c_{cr} = 2m\omega = 2\sqrt{km}$ )                          |
| $f$        | Frequency (in Hz)<br>External forcing frequency  |
| $f_d$      | Natural frequency of the damper<br>Nonlinear natural frequency of the TLD: $f_d = \xi f_w$ |
| $f_e$      | External forcing frequency   |
| $f_{jump}$ | Jump frequency   |
| $f_w$      | Linear natural frequency of the TLD based on linear theory                                 |
| $g$        | Gravity acceleration   |

|                    |   |
|--------------------|---|
| $h_0$              | Undisturbed water depth   |
| $k$                | Stiffness coefficient   |
| $k_d$              | Stiffness of the damper   |
| $k_w$              | Fundamental linear stiffness of the TLD   |
| $m$                | Mass  |
| $m_d$              | Mass of the damper  |
| $m_s$              | Mass of the structure   |
| $m_w$              | Mass of the water   |
| $u$                | Horizontal velocity of water particles  |
| $x$                | Absolute displacement of the structure  |
| $\bar{x}$          | Relative displacement of the structure  |
| $x_0$              | Maximum displacement of the structure without damper<br>Initial displacement of the structure in free vibration |
| $x_s$              | Structural displacement   |
| $x_d$              | Damper's displacement   |
| $\Lambda$          | Nondimensional excitation amplitude ( $A/L$ )   |
| $\beta$            | Excitation frequency ratio ( $\beta = f_e / f_s$ )  |
| $\beta_d$          | Damper frequency ratio to external forcing frequency  |
| $\beta_{jump}$     | Jump frequency ratio ( $\beta_{jump} = f_{jump} / f_w$ )  |
| $\varepsilon$      | Water depth ratio ( $\varepsilon = h/L$ )   |
| $\phi$             | Phase angle   |
| $\gamma$           | Damper frequency ratio ( $f_d/f_s$ )  |
| $\eta$             | Wave height or free water surface elevation   |
| $\kappa$           | Stiffness hardening ratio or non-dimensional stiffness of damper  |
| $\mu$              | Mass ratio ( $m_d/m_s$ )  |
| $\omega, \omega_e$ | External forcing angular frequency  |
| $\omega_s$         | Excitation angular frequency of shaking table   |

|            |   |
|------------|---|
|            | Natural angular frequency of structure          |
| $\omega_d$ | Natural angular frequency of damper             |
| $\omega_w$ | Fundamental linear angular frequency of the TLD |
| $\xi$      | Frequency shift ratio                           |
| $\zeta$    | Damping ratio ( $\zeta = c/c_{cr}$ )            |
| $\zeta_s$  | Damping ratio of structure                      |
| $\zeta_d$  | Damping ratio of damper                         |

#### Superscripts

|           |                                 |
|-----------|---------------------------------|
| $a'$      | Nondimensionalized value of $a$ |
| $\dot{a}$ | Time derivative of $a$          |

#### Subscripts

|     |           |
|-----|-----------|
| $d$ | Damper    |
| $e$ | External  |
| $s$ | Structure |

|      |  |
|------|--|
| DOF  | Degree Of Freedom                                  |
| NSD  | A SDOF System with Nonlinear Stiffness and Damping |
| RCM  | Random Choice Method                               |
| RMS  | Root Mean Square                                   |
| SDOF | Single Degree Of Freedom                           |
| TLD  | Tuned Liquid Damper                                |
| TMD  | Tuned Mass Damper                                  |

## ACKNOWLEDGMENTS

I would like to thank Professor Dorothy A. Reed for providing the opportunity to perform this research. Without her valuable guidance and continuous support through the long process of research, this dissertation would not have been possible.

I wish to extend my sincere appreciation to Professor Harry Yeh. His sharp insight into the subject always guided me to the right track of the research.

Appreciation is also directed to Professors Gregory Miller and George Turkiyyah for their thorough review of this dissertation in a timely manner. Their comments and suggestions significantly improved this document.

Most of all, my gratefulness is to my wife Myung, son Jeehah and daughter Jean for their love, support and patience.

## CHAPTER 1

### INTRODUCTION

Undesirable vibrations of lightly damped, flexible modern structures have created concern in the structural engineering community. Although these vibrations are related to serviceability problems, such as occupant comfort and cladding integrity, rather than affecting the primary load-bearing capacity, the economic considerations are significant. The most promising solution to mitigating these vibrations is through the use of artificial damping devices.

In recent years, one type of passive damping system, called the tuned liquid damper (TLD) has been successfully employed in practice, e.g., Fediw, et al. (1993); Fujii, et al. (1990); Tamura, et al. (1988); Ueda, et al. (1991); Wakahara, et al. (1992, 1993). Although this type of device has many advantages, the mechanism by which it dissipates energy related to undesirable vibrations is not completely understood, nor has it been thoroughly investigated. The primary objective of this study is to investigate experimentally and numerically the behavior of tuned liquid dampers in order not only to identify the underlying physical phenomenon of the liquid sloshing behavior that contributes to the damping capability of the device, but also to incorporate such knowledge into the development of a design scheme.

In this chapter, a review of background information for this study will be presented. Following this review, an outline of the organization of this dissertation is provided.

#### **1.1 Tuned liquid damper (TLD)**

The tuned liquid damper is a passive mechanical damper designed to suppress undesirable structural vibration through the liquid sloshing motion in a rigid tank. The vibration energy is dissipated by means of friction in the boundary layers of the fluid,

contamination of the free surface and wave breaking. Water is most commonly used as a liquid for the TLD, hence, the words “water” and “liquid” are used interchangeably throughout this study.

For analysis purposes, the water in rigid tanks is classified as “deep” or “shallow”. The specific classification is based on the ratio of the water depth to the wave length in the direction of motion. The damping mechanism in the water is developed primarily by the viscous action in the boundary layers near the bottom surface and the side walls of the tank and the sloshing motion of the free surface layer of the water. As a damper, deep water is limited in its damping capability because a large portion of the water does not participate in the damping mechanism. Shallow water maximizes the participation of the water in the damping action. This research focuses on the TLD using shallow water.

The motion of liquids in rigid containers has been a subject of many studies due to its frequent applications in engineering disciplines, e.g., Chaiseri, et al. (1989); Chester, et al. (1968); Faltinson, et al. (1978); Housner (1959); Lepelletier (1988); Miles (1976); Modi, et al. (1988); Shimizu, et al. (1987). Notable progress in numerical simulation of the shallow water for the rectangular TLD was made by Sun (1992). Because his analytical model can not simulate the water sloshing motion with wave breaking, he introduced two empirically-based coefficients for damping and frequency shift in the governing equations. Koh et al. (1994) modified Sun’s model to make the energy dissipation term applicable to arbitrary excitations. Gardarsson and Yeh (1994) proposed a numerical solution scheme to solve the shallow-water equations using the random choice method (RCM).

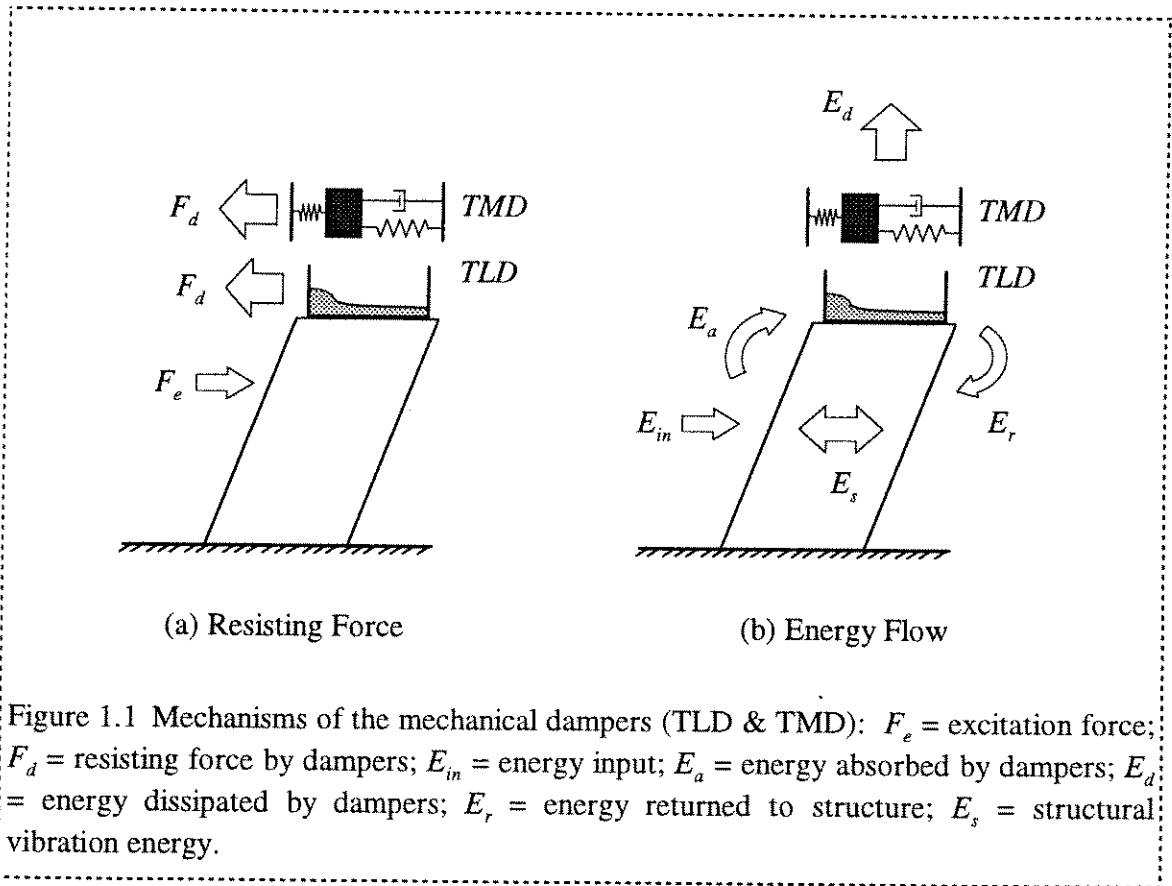
Recently, successful applications of TLDs to civil engineering structures have been reported. It was found that the TLD has several potential advantages over other damping systems, such as low installation and maintenance cost; fewer mechanical problems; no fail-safe devices required; activated at even low excitation levels; and easy adjustment of the damper parameters even after installation by adjusting the water level in the tank. This result implies a promising future of TLD as a damping device for various types of civil

engineering structures including super flexible tower-type structures and high-rise buildings. It is also noted that there exist difficulties in TLD design because of the complex behavior of liquid sloshing that involves a consideration of wave breaking and amplitude dependent nonlinear characteristics.

## 1.2 Damping mechanism of the TLD

In this section, the damping mechanism of the TLD is reviewed. Because the tuned mass damper (TMD) is a well-known passive mechanical damping system that has been used widely for serviceability-based structural vibration control, the damping mechanism of the TMD is continuously referenced in explanations of the TLD.

Figure 1.1 demonstrates schematics of passive mechanical dampers (TLD & TMD)



attached to a structure. Figure 1.1(a) schematically illustrates the inertia forces of the solid mass in the TMD and the water mass in the TLD resisting structural motion as the structure is subjected to an external force. Figure 1.1(b) presents the energy flow among the excitation force, the structure and the damper. The dampers absorb a part of the structural vibration energy. The absorbed energy is dissipated through the damper's inherent damping capacity. The energy flow from the structure to the damper is called the "energy absorption mechanism". The damper changes the dynamic characteristics of the structure by changing the phase of the structural motion through the absorption mechanism. The structural vibration energy is dissipated through the energy dissipation capacity of the damper.

The motion of the solid mass and the characteristics of the stiffness and damping of the TMD have been thoroughly investigated. However, the motion of the water mass and the characteristics of the stiffness and damping of the TLD have not been subject to the same level of scrutiny. In particular, as the wave breaking occurs, the water sloshing motion cannot be predicted by analytical methods.

### 1.3 Performance measurement of damping devices

The ultimate goal of this research is to develop a design process for the TLD. The design criteria must be evaluated in the context of damper performance. Performance of the damper is defined as the capability to reduce undesirable structural motion effectively and robustly. Effectiveness of the damper may be assessed in several ways, including one or more of the following (Reed, et al., 1996):

- Reduction in peak or RMS structural displacement;
- Reduction in peak or RMS structural acceleration;
- Increase in "effective damping" of the combined system when the main system coupled with the damper is treated as a single-degree-of-freedom combined system; or
- Increase in energy dissipation per cycle over a system without a damping device.

Performance of the damper in terms of robustness is another important consideration in damper design. Robustness of the damper performance is not a well-defined term. However, in general, it would be qualitatively defined as “the level of insensitivity of the damper effectiveness to slight offsets in damper parameters from the desired values.” The damper parameters in this sense include, but are not limited to, the tuning and damping ratios of the damper. The offset in the damping parameters occurs mainly due to the inaccurate estimations of the structural properties, damper properties, mass ratio, or loading conditions. In this research, the robustness of the TLD will be assessed in the context of energy dissipation over a wide range of excitation frequencies.

#### **1.4 Objectives and scope of work**

Despite several successful applications as well as numerical and experimental investigations of the TLD behavior, there currently exist limitations which restrict the designer’s ability to effectively employ the TLD as a damping device. These limitations include, but are not limited to, the following:

- The underlying physical phenomenon of the water sloshing motion is not thoroughly understood. Although the wave breaking phenomenon is common in real practice, water sloshing with wave breaking has rarely been addressed in research. Some important characteristics of shallow water sloshing motion such as nonlinearity have been identified but not explicitly quantified.
- Present methods for TLD design involve many approximations and there are no definitive guidelines.

In recognition of these limitations, the primary objectives of this study were established as follows:

- To investigate the characteristics of the shallow water sloshing motion in a tank using shaking table experiments under small and large amplitude excitations.

- To explicitly identify and quantify parameters which significantly influence the TLD performance.
- To develop a simple mechanical model of the TLD based on the experimental results.
- To identify a numerical fluid model based on the shallow-water equations for use in prediction of tank behavior.
- To develop a design procedure for the TLD.

In this thesis, background theory and results of the experimental investigations will be presented prior to the numerical models. Design procedures and their applications under various loading conditions will be discussed.

Chapter 2 presents the results of experimental investigations of the characteristics of shallow water waves in rectangular and circular tanks. The behavior of wave breaking in rectangular tanks is examined in detail. Because structural vibration is not purely uni-axial motion, circular TLDs may be more feasible than rectangular ones. The characteristics of wave motion in circular tanks are discussed based on the experimental results.

In Chapter 3, an equivalent TMD model of a TLD of rectangular or circular shape is proposed. This model possesses nonlinear stiffness and damping calibrated from the experimental investigations. This model is called the NSD model because of the nonlinear stiffness and damping parameters. An energy dissipation matching scheme used to identify these parameters will be described in detail. A numerical scheme to solve the shallow-water wave equations using the random choice method (RCM model) proposed by Gardarsson and Yeh (1994) will be evaluated based on the experimental results.

In Chapter 4, numerical schemes to model the interaction of a TLD with a single-degree-of-freedom structure are developed. The capability and limitations of the RCM model are evaluated. Frequency response analysis methods coupled with an iterative procedure to solve the nonlinear system are developed for harmonic or white noise excitations. Performance of the TLD is evaluated using the solution scheme. A dynamic

searching scheme for the effective TLD design is proposed. Performance of TLDs under wind or earthquake conditions is investigated. Wind pressure time series data were generated using an autoregressive model. Ground displacement data for Northridge earthquake were selected for the study. Conclusions of the research are summarized in Chapter 5.

## CHAPTER 2

### EXPERIMENTAL INVESTIGATIONS OF SHALLOW WATER WAVES IN RECTANGULAR AND CIRCULAR TANKS

A series of shaking table experiments were conducted to investigate the characteristics of water sloshing motion in rectangular and circular tanks under various base excitation conditions. The results for harmonic base excitation are presented in this chapter. The results for earthquake conditions will be discussed in Chapter 4.

#### 2.1 Shaking table tests

##### 2.1.1 Test set-up

Figure 2.1 shows the schematic diagram of the shaking table experiment set-up. The experiment was conducted using the facilities in the structural dynamics laboratory at the University of Southern California. The components of the experimental set-up are described below:

- 1) Shaking Table: The MTS shaking table can generate a horizontal motion in one direction. The shaking table has capacities of  $\pm 51$  mm maximum displacement, 890 mm/sec maximum velocity, 4g maximum acceleration, and 0 to 50 Hz operating frequency. The amplitude and the frequency of the harmonic shaking table excitation was controlled manually using the console panel. The feed-back signal from the actuator is recorded as the shaking table displacement,  $x_s$ .
- 2) Loadcell: The multi-component transducer can measure six directional components of force/moment. The loadcell was calibrated on site under static and dynamic loads.

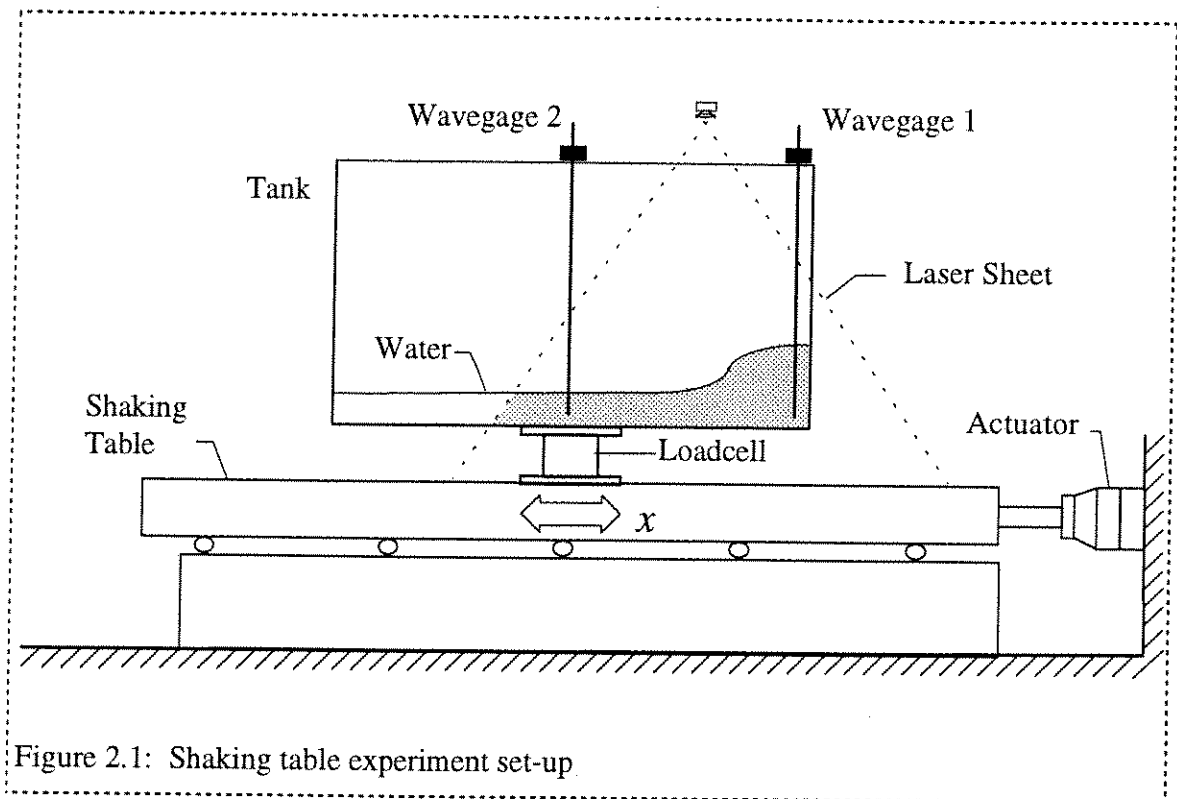


Figure 2.1: Shaking table experiment set-up

3) Wavegauge: Capacitance-type wave gages were installed near the end wall, at the mid-tank<sup>\*1</sup> and at the middle of the side wall of the circular tank. The gages near the wall are located at 17 mm and 40 mm from the inside surface of the tank wall for the rectangular tank and the circular tank respectively.

4) Laser-light sheet: A higher-power (4W) Argon-ion laser projects a laser beam. The laser beam is directed through fiber-optics and converted to a thin laser sheet by a scanner. The image of the vertical laser-sheet illumination through the water depth is captured by a video camera and processed with a microcomputer. The quantitative video visualization allows for analysis of the spatial, as well as temporal, variations of the water surface profiles.

<sup>\*1</sup> In the shortest tank ( $L=335$  mm), wave gage was installed only at the end wall because there was no space for mounting. For the circular tank, an additional wave gage was installed at the middle of the side wall.

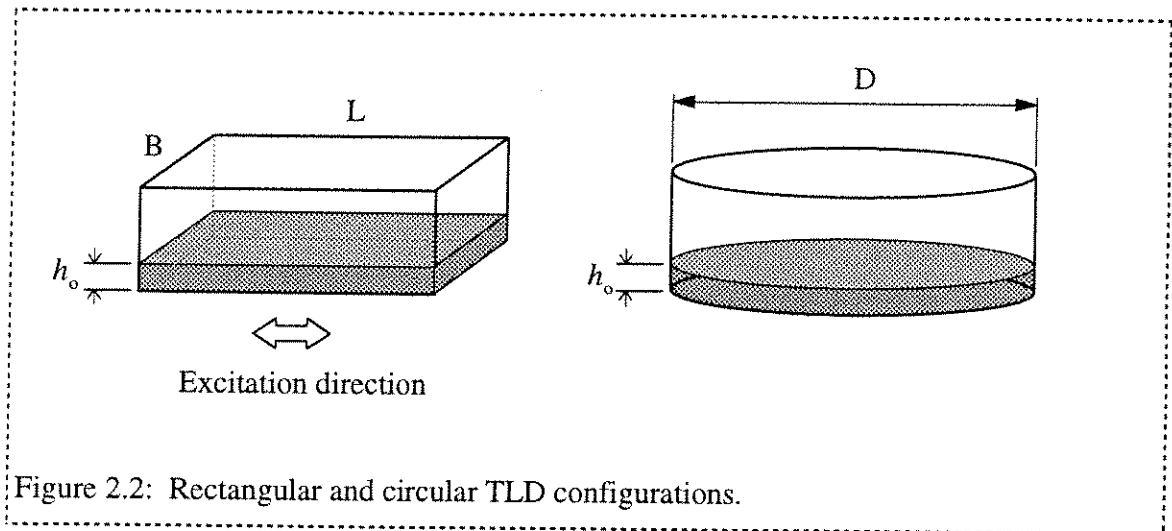


Figure 2.2: Rectangular and circular TLD configurations.

- 5) A harmonic function generator was connected to the actuator to control the motion of the actuator. The data were collected using a 16 channel data acquisition system.
- 6) Tank: The tanks were fabricated from clear acrylic plates. The bottom plates of the tanks are 19 mm ( $\frac{3}{4}$ " ) thick. The side plates are 13 mm ( $\frac{1}{2}$ " ) thick for the rectangular tanks and 6 mm( $\frac{1}{4}$ " ) thick for the circular one. Water was used for these experiments. The configurations of the tanks are illustrated in Figure 2.2 and described in Tables 2.1 and 2.2.

### 2.1.2 Test cases

One of the primary objectives of the experimental study was to investigate the behavior of the water sloshing motion and the effects of the excitation amplitudes and frequencies, tank configurations and liquid depth on the sloshing behavior. Three different sizes of rectangular tanks and one circular tank were investigated in the study. The rectangular tank sizes were selected on the basis of previous investigations for rectangular tanks by Sun, et al. (1991) and Koh, et al. (1994). The circular tank size was selected to maintain the fundamental natural frequency of the water sloshing with the same depth of water as one of the rectangular tanks. Each tank filled with the desired level of water was

excited with various amplitudes and frequencies as described in Tables 2.1 and 2.2. The data were recorded after the water sloshing motion reached the steady state.

Based on the linear wave theory (Lamb, 1932), the fundamental natural frequency of the water sloshing motion,  $f_w$ , was calculated by

$$f_w = \frac{1}{2\pi} \sqrt{\frac{\pi g}{L} \tanh\left(\pi \frac{h_0}{L}\right)} \quad \text{for a rectangular tank} \quad (2.1)$$

Table 2.1: Data for the experimental investigations of rectangular tanks.

| Tank Size             |                      | Water Depth<br>$h_0$<br>(mm) | Water Depth Ratio<br>$\epsilon$ | Natural Freq.<br>$f_w$<br>(Hz) | Excitation Amplitude |             |
|-----------------------|----------------------|------------------------------|---------------------------------|--------------------------------|----------------------|-------------|
| Length<br>$L$<br>(mm) | Width<br>$b$<br>(mm) |                              |                                 |                                | $A$<br>(mm)          | $A/L$       |
| 335                   | 203                  | 9.6                          | 0.029                           | 0.457                          | 10,20,40             | .030 - .119 |
| 335                   | 203                  | 15                           | 0.045                           | 0.571                          | 2.5,5,10,20,30       | .007 - .119 |
| 590                   | 335                  | 15                           | 0.025                           | 0.325                          | 2.5,5,10,20,30,40    | .004 - .068 |
| 590                   | 335                  | 22.5                         | 0.038                           | 0.397                          | 2.5,5,10,20,30,40    | .004 - .068 |
| 590                   | 335                  | 30                           | 0.051                           | 0.458                          | 2.5,5,10,20,30,40    | .004 - .068 |
| 590                   | 335                  | 45                           | 0.076                           | 0.558                          | 20                   | .034        |
| 900                   | 335                  | 30                           | 0.033                           | 0.301                          | 2.5,5,10,20,30,40    | .003 - .044 |
| 900                   | 335                  | 40                           | 0.044                           | 0.347                          | 2.5,5,10,20,30,40    | .003 - .044 |
| 900                   | 335                  | 55                           | 0.061                           | 0.406                          | 10,20                | .011 - .022 |
| 900                   | 335                  | 71                           | 0.079                           | 0.459                          | 2.5,5,10             | .003 - .011 |

Table 2.2: Data for the experimental investigations of circular tanks

| Tank Diameter<br>$D$<br>(mm) | Water Depth<br>$h_0$<br>(mm) | Water Depth Ratio<br>$\epsilon$ | Natural Freq.<br>$f_w$<br>(Hz) | Excitation Amplitude |             |
|------------------------------|------------------------------|---------------------------------|--------------------------------|----------------------|-------------|
|                              |                              |                                 |                                | $A$<br>(mm)          | $A/D$       |
| 690                          | 15                           | 0.022                           | 0.325                          | 10,20,40             | .014 - .058 |
| 690                          | 22.5                         | 0.033                           | 0.397                          | 10,20,40             | .014 - .058 |
| 690                          | 30                           | 0.043                           | 0.458                          | 2.5,5,10,20,30, 40   | .004 - .058 |
| 690                          | 40                           | 0.065                           | 0.558                          | 2.5,5,10             | .004 - .014 |

and

$$f_w = \frac{1}{2\pi} \sqrt{\frac{1.17\pi g}{D} \tanh\left(\frac{1.17\pi h_0}{D}\right)} \quad \text{for a circular tank} \quad (2.2)$$

where  $g$  is gravity acceleration,  $L$  and  $D$  are the length and the diameter of the tank, respectively, and  $h_0$  is the undisturbed water depth as illustrated in Figure 2.2.

## 2.2 Characteristics of water sloshing motion in rectangular tanks

In presenting the experimental results, several key parameters will be used. These are defined as follows:

The wave height,  $\eta$ , is defined as the water surface elevation from the undisturbed state. In the experiments, it was measured by wave gages near the end wall, at the mid-tank (when possible) and at the middle of the side wall (for the circular tank only). The quantity is nondimensionalized by dividing by the undisturbed water depth,  $h_0$ , as

$$\eta' = \frac{\eta}{h_0}. \quad (2.3)$$

The base shear force,  $F_w$ , is defined as the reaction force of the water tank created by water sloshing motions induced by the shaking table movement. In this analysis, the measured base shear force was obtained by subtracting the inertia force of the tank from the total force measured by the loadcell to identify the force due to water sloshing motion only. In order to eliminate the undesirable high-frequency system noise, which is always present in the laboratory data, a low-pass filter was applied to the measured data. The applied low-pass filter will be discussed later in this section. The base shear force is nondimensionalized as

$$F'_w = \frac{F_w}{m_w \omega^2 A} \quad (2.4)$$

where  $m_w$  is the mass of the water in the tank,  $\omega$  is the excitation angular frequency of the shaking table,  $A$  is the shaking table excitation amplitude and the product  $m_w \omega^2 A$  is the maximum inertia force of the water mass treated as a solid mass.

The amount of energy dissipation per cycle is an important concern for vibration control. As will be seen in the interaction model of Equation (4.1), the base shear force,  $F_w$ , generated by the water sloshing motion resists the excitation motion. Therefore, a measure of this force in dissipating energy is critical to this investigation. The energy dissipation per cycle,  $E_w$ , is defined as the work done by the base shear force during one cycle of the shaking table motion. This quantity is represented by the area of force-displacement ( $F_w - x_s$ ) loop which can be calculated by

$$E_w = \int_{T_s} F_w dx_s \quad (2.5)$$

where  $T_s$  is the period of the shaking table motion and  $x_s$  is the shaking table displacement. The energy dissipation per cycle is nondimensionalized as

$$E'_w = \frac{E_w}{\frac{1}{2} m_w (\omega A)^2} \quad (2.6)$$

where  $m_w (\omega A)^2 / 2$  is the maximum kinetic energy of the water mass treated as a solid mass. In the next section, an examination of these parameters is presented for the experimental cases.

In the data analyses, a low-pass filter<sup>1</sup> was employed to eliminate the high-frequency system noise or to separate each frequency component of waves. The natural fundamental frequency of the empty tank system which comprises the empty tank, the loadcell and the mounting system was identified at approximately 10 Hz. The noise from the shaking table

---

<sup>1</sup> Zero-phase forward and reverse digital filtering technique was employed using 5<sup>th</sup> order low-pass digital Butterworth filter. Refer to Matlab commands "BUTTER" and "FILTfilt" in signal processing toolbox.

system was measured at much higher frequencies. To eliminate the high-frequency system noises, the cut-off frequency of the low-pass filter must be set to a lower value than 10 Hz: e.g., the cut-off frequency was set to 5 Hz for the loadcell-measured base shear data along the excitation direction. For shallow water in a rectangular tank, the natural frequencies of each mode of the sloshing motion can be expressed as

$$f_n \approx n f_1 \quad (2.7)$$

where the subscripts indicate the mode number and  $f_1$  is the fundamental natural frequency that can be calculated from Equation (2.1). To identify the effect of each mode of water sloshing motions, it is necessary to filter out all frequency components higher than the designated frequency. This filter-out was done by adjusting the cut-off frequency of the low-pass filter to a desired value: e.g., to obtain the data including up to  $n^{\text{th}}$  mode, the cut-off frequency of the low-pass filter was set to  $(n+0.5)$  times the fundamental natural frequency, i.e., *cut-off frequency* =  $(n+0.5) f_1$ .

### 2.2.1 Time history responses of water sloshing motion at steady-state for harmonic excitation

Figure 2.3 shows the sample time history responses of the steady-state water sloshing motions for the rectangular tank of length  $L = 590$  mm, water depth  $h_0 = 30$  mm and excitation amplitude  $A = 20$  mm at the harmonic base excitation frequency ratios  $\beta = 0.7, 1.0, 1.2$  and  $1.4$ , respectively. The excitation frequency ratio in the horizontal axis is defined as

$$\beta = \frac{f_e}{f_w} \quad (2.8)$$

where  $f_e$  is the shaking table excitation frequency and  $f_w$  is the fundamental natural frequency of water sloshing calculated with Equations (2.1) or (2.2). In the figure,  $\eta'_1$  and  $\eta'_2$  are the nondimensional wave heights near the end wall and at the middle of the tank, respectively.  $F_{wx}$  and  $F_{wy}$  are the base shear force measured along and across the direction

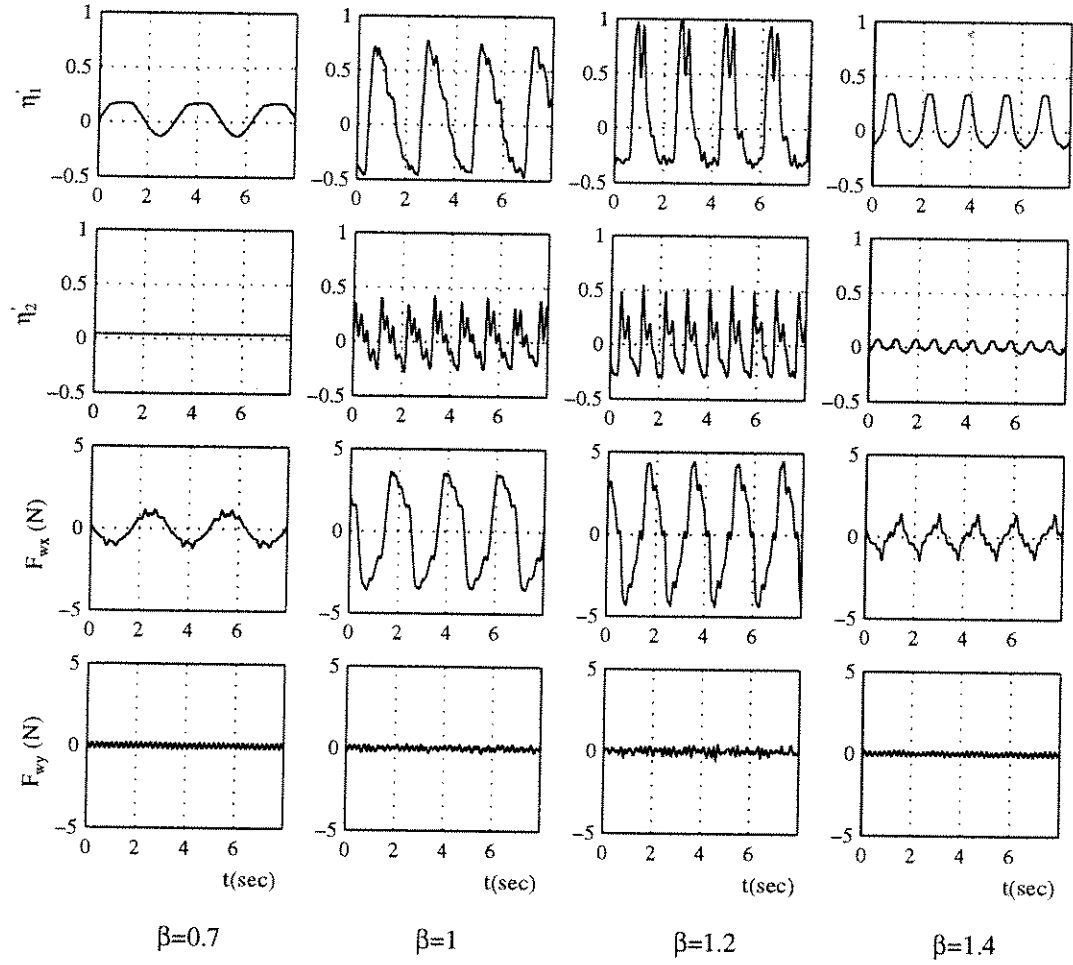


Figure 2.3 Sample time histories of water sloshing motions in the shaking table tests for the case of the tank with length  $L=590$  mm, water depth  $h_0=30$  mm, and excitation amplitude  $A=20$  mm; the water surface elevation at the end wall  $\eta_1'$  and at the mid-tank  $\eta_2'$  and the base shear forces  $F_{wx}$  and  $F_{wy}$  in the direction of along and across excitation, respectively.  $\beta$  is the excitation frequency ratio.

of excitation, respectively. The raw data measured with the loadcell contain system noise. As will be discussed in Section 2.2.3, contribution of the frequency-components higher than 5 Hz on the wave motion is not significant and can be ignored. Therefore, a low-pass filter with cut-off frequency of 5 Hz was applied to the raw data of  $F_{wx}$  to eliminate the system noise. The raw data of  $F_{wy}$  are filtered by a low-pass filter with cut-off frequency of 10 Hz. At the excitation frequency ratio  $\beta = 0.7$ , small and smooth waves develop. At higher excitation frequency ratios  $\beta$  of 1.0 and 1.2 which are near the fundamental natural frequency of the TLD, strong waves develop and wave breaking occurs. In this range of excitation frequencies, higher-frequency waves riding on the primary wave appear in the wave motion. The wave motion dramatically decreases at  $\beta = 1.4$ .

Figure 2.4 presents the steady-state time history responses of the water surface elevations at the end wall,  $\eta'_1$ , for the case of the tank with length  $L = 590$  mm and water depth  $h_0 = 30$  mm at various excitation frequencies for the excitation amplitudes  $A = 10, 20$  and  $40$  mm, respectively. Wave breaking was apparent over a wide range of frequencies for each excitation amplitude case. High-frequency waves are evident in the wave motions. The high-frequency components of the wave decrease at larger amplitude excitation. The wave shapes show significant irregularities. The irregularities become more significant as the excitation amplitude increases and are taken into account in the data analyses. It is apparent that the water sloshing motion changes depending on the excitation amplitude and frequency.

Figure 2.5 illustrates the loadcell-measured base shear force due to water sloshing motions,  $F_w$ , for the same cases as Figure 2.4. The irregularities previously observed in the wave height measurements are not significant for the base shear force data. The influence of high-frequency waves is less significant on the base shear force than on the wave height. The high-frequency waves decrease as the excitation amplitude increases.

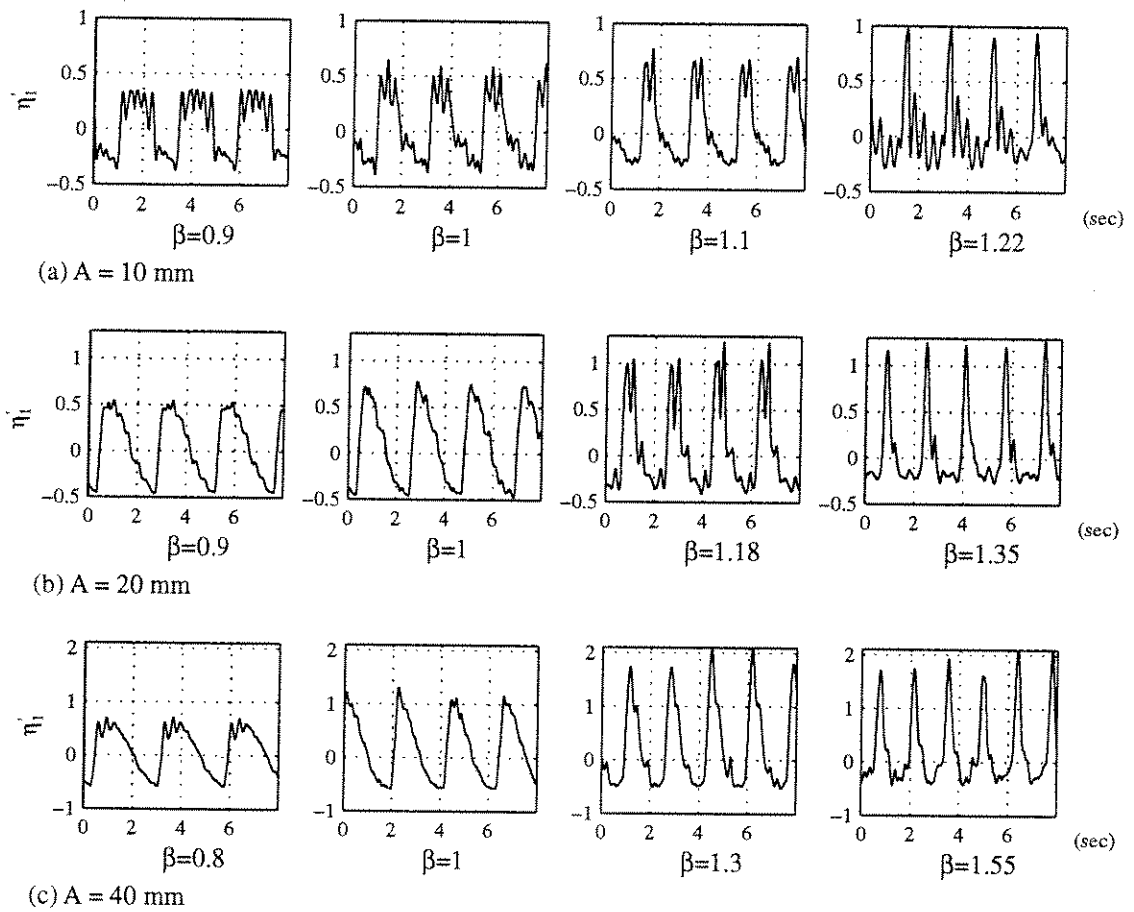


Figure 2.4 Sample time histories of the nondimensional wave heights for the steady-state wave motion at various excitation frequencies for the cases of the tank with length  $L = 590$  mm, water depth  $h_0 = 30$  mm and excitation amplitude  $A = 10, 20$  and  $40$  mm, respectively.

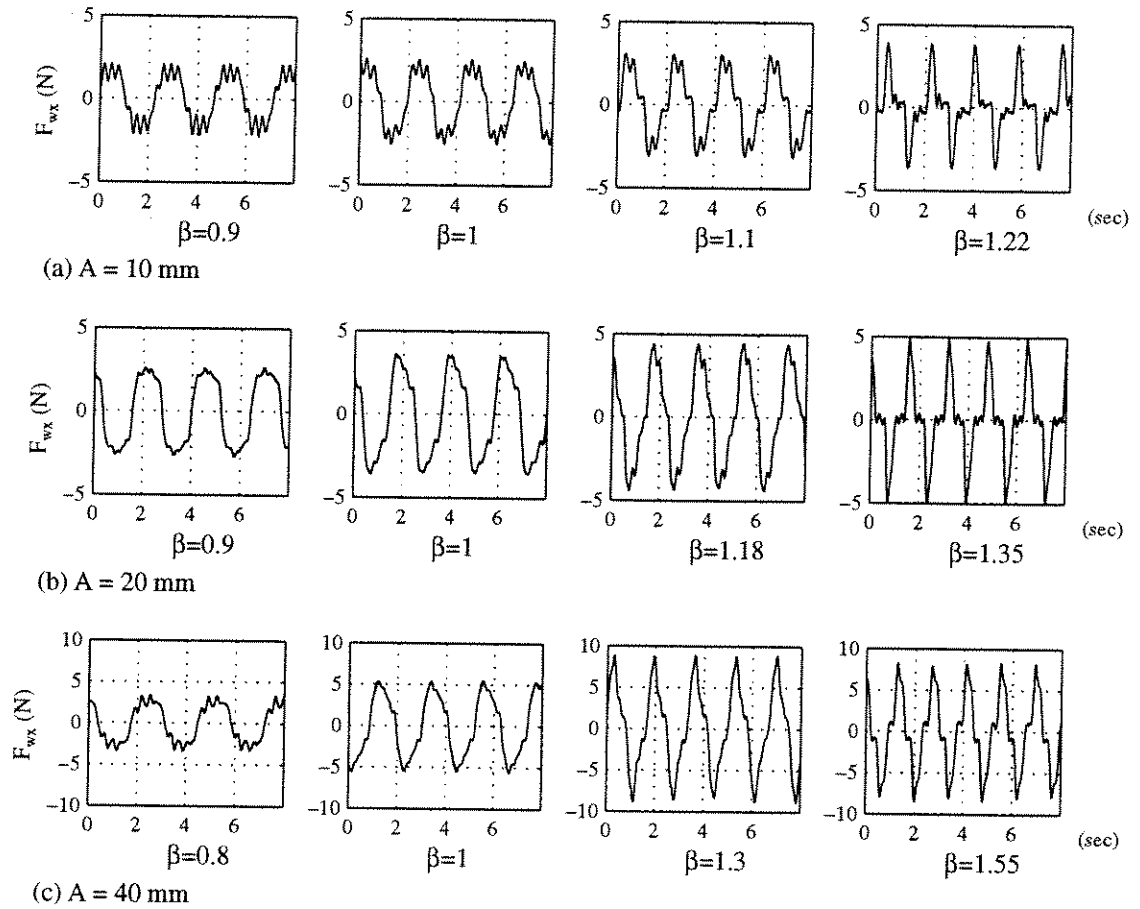


Figure 2.5 Sample time histories of the measured base shear force in the  $x$ -direction for the same conditions as Figure 2.4.

Figure 2.6 contains plots of the base shear force vs. the shaking table displacement ( $F_w$ - $x_s$  loops) for the same cases as in Figure 2.5. The dashed lines indicate the base shear forces including only the fundamental mode of water sloshing. The solid lines indicate the base shear forces including higher modes up to 5<sup>th</sup> mode. The effects of the higher modes of water sloshing motions on the time history base shear forces can be determined by comparing these two curves. The higher modes change the time history of the magnitude of the base shear forces. However, the amount of the energy dissipation per cycle which is calculated by the area inside the loop does not change significantly by the higher modes. For example, for the sweep frequency cases of the tank with length  $L=590$  mm, water depth  $h_0 = 30$  mm and excitation amplitude  $A = 20$  mm, the difference in the energy dissipation using the two representations is on average about 2 %. As mentioned in Chapter 1, the energy dissipation capacity is a measurement of the performance of tuned liquid dampers. The magnitude of the base shear force  $|F_w|$  and its phase lag  $\phi$  from the shaking table displacement are two major factors determining the area inside the contour. The time history magnitudes of the base shear forces during one cycle can be most accurately represented by the RMS values.

### 2.2.2 Frequency responses of water sloshing motion

As observed in the study of time history responses in the previous section, the characteristics of water sloshing in the tank depend on the base excitation amplitude  $A$ , the tank length  $L$ , and the water depth  $h_0$ . The three primary parameters may be combined to define the secondary parameters: the linear fundamental natural frequency  $f_w$ , the base excitation amplitude in acceleration  $\ddot{A}$ , and the water depth ratio  $\varepsilon$ . The linear fundamental natural frequency  $f_w$  is defined in Equations (2.1) or (2.2). The base excitation amplitude in acceleration is defined as  $\ddot{A} = \omega_e^2 A$  in which  $\omega_e = 2\pi f_e = 2\pi\beta f_w$ . The water depth ratio is defined as  $\varepsilon = \frac{h_0}{L}$ . The effects of each parameter on the water sloshing motions are investigated and discussed in this section.

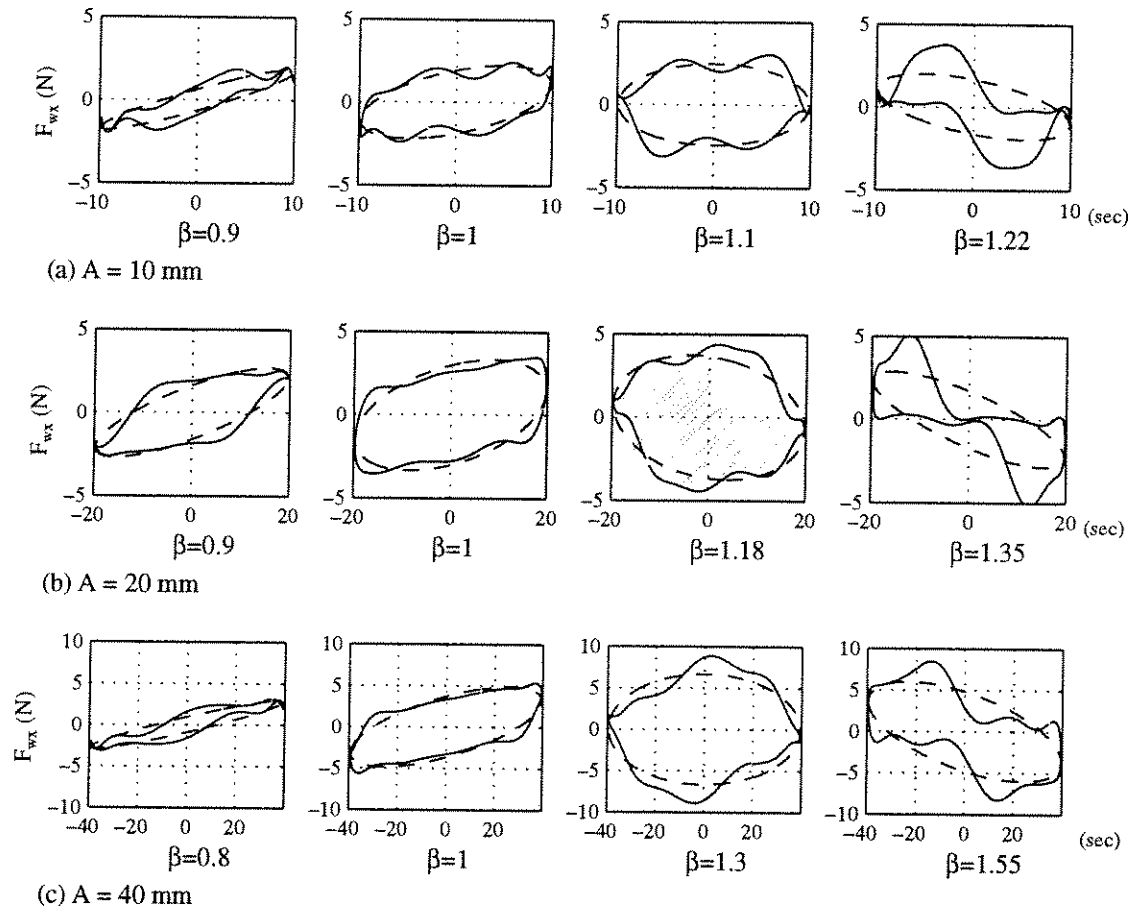


Figure 2.6 Energy dissipation curves of the base shear force  $F_w$  vs. the shaking table displacement  $x_s$  for the same conditions as Figure 2.5. The dashed lines represent calculations including higher modes up to 9<sup>th</sup> mode; the solid line represents calculations only including the first mode.

To investigate the effects of the base excitation amplitude upon wave motion in the tank, the experimental cases of the tank with length  $L = 590$  mm, water depth  $h_0 = 30$  mm are examined under various excitation amplitudes  $A = 10, 20$  and  $40$  mm. Figure 2.7 shows the frequency sweep plots of several nondimensional quantities: the maximum wave height near the end wall  $\eta'_{1,\max}$ , the maximum base shear force  $F'_{w,\max}$ , the phase angle  $\phi$  of the fundamental mode of  $F_w$  from  $x_s$ , and the energy dissipation per cycle  $E'_w$ .

The maximum wave height increases as the excitation frequency increases toward the fundamental natural frequency of the TLD. The wave height reaches peak value at the excitation frequencies higher than the fundamental natural frequency, i.e.,  $\beta > 1.0$ . This phenomenon illustrates the nonlinear characteristics of the water sloshing motions. After a gradual, fairly smooth build-up to a peak value, at a certain excitation frequency, the value of  $\eta'_{1,\max}$  drops dramatically. This excitation frequency is referred to as the “jump frequency”,  $f_{\text{jump}}$ , and used as a parameter representing the nonlinearity of the wave motion. The existence of the jump frequency at  $\beta > 1.0$  indicates that the water sloshing motion displays a “hardening-spring type” nonlinearity. As the excitation amplitudes increase from  $A=10$  mm to  $A=40$  mm, the jump frequency ratios increase from about 1.22 to 1.55, where the jump frequency ratio is defined as  $\beta_{\text{jump}} = \frac{f_{\text{jump}}}{f_w}$ . This indicates that the nonlinearity of the water sloshing motion becomes stronger as the excitation amplitude increases. In summary, as the base excitation amplitude increases:

- The resonance frequency increases.
- The peak value of the maximum wave height increases over all frequencies.
- The magnitudes of the base shear and the energy dissipation increase. However, the nondimensional maximum base shear and the corresponding nondimensional energy dissipation per cycle decrease.

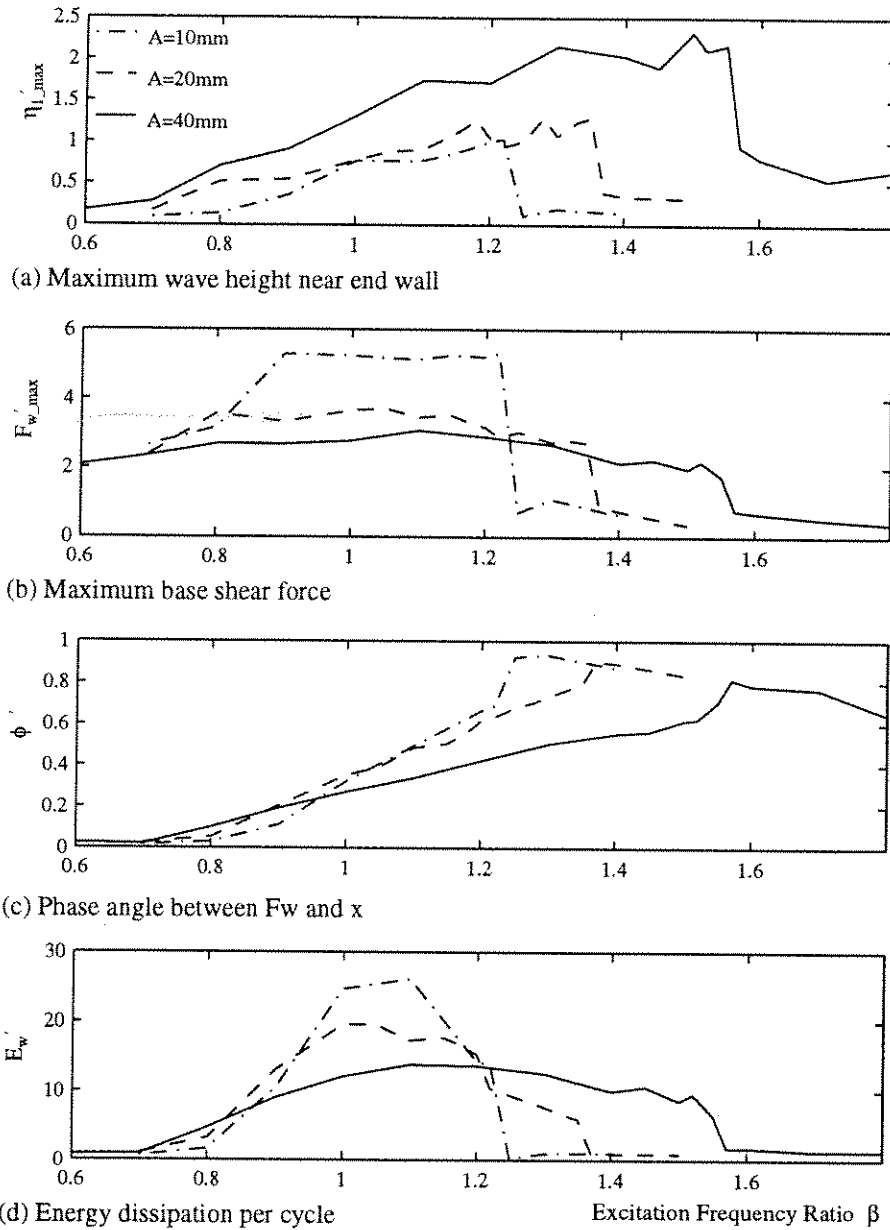


Figure 2.7 Sample frequency responses of water sloshing motion in shaking table tests of the tank with length  $L = 590$  mm, water depth  $h_0 = 30$  mm and excitation amplitude  $A = 10, 20$  and  $40$  mm.

- The slope of phase angle curve decreases over sweep excitation frequencies.
- The region of excitation frequencies at which the water sloshing motion is active becomes wider.

Figure 2.8 presents two sweep frequency plots of the maximum wave heights at the end wall of the tank  $\eta_{1,\max}$  to investigate the effect of the water depth  $h_0$  upon the water sloshing motion in the tank. The two primary parameters  $A$  and  $L$  are fixed while the water depth  $h_0$  varies. Figure 2.8(a) shows the frequency responses of the tank with length  $L = 590$  mm with water depth  $h_0 = 15, 22.5, 30$  and  $45$  mm respectively under the excitation amplitude  $A = 20$  mm. Figure 2.8(b) presents the same plots of the tank with length  $L = 900$  mm with water depth  $h_0 = 40, 55$  and  $71$  mm under the excitation amplitude  $A = 10$  mm. Although slight variations in the shape and magnitude of the curves are observed, the water depth does not significantly influence the water sloshing motion in the range of selected experimental cases.

Figure 2.9 contains the sweep frequency plots of the maximum wave heights at the end wall of three tanks with lengths  $L = 335, 590$  and  $900$  mm, respectively for excitation amplitude  $A = 10$  mm. The water depth of each tank was determined such that the linear fundamental natural frequencies  $f_w$  of the tanks become identical: in this case  $f_w = 0.458$  Hz. It is observed that the smaller tank with the shallower water depth develops the stronger wave motion and the higher jump frequency. Because the effect of the water depth is not significant as observed in Figure 2.8, the differences in three curves reflect mainly the influence of the tank length  $L$  on the wave motion. Apparently, the length of the tank influences the water sloshing motion significantly.

The data shown in Figures 2.7 through 2.9 indicate that the water sloshing motion in the tank is significantly influenced by the excitation amplitude and the tank length. The underlying physical phenomenon is described in the following paragraphs.

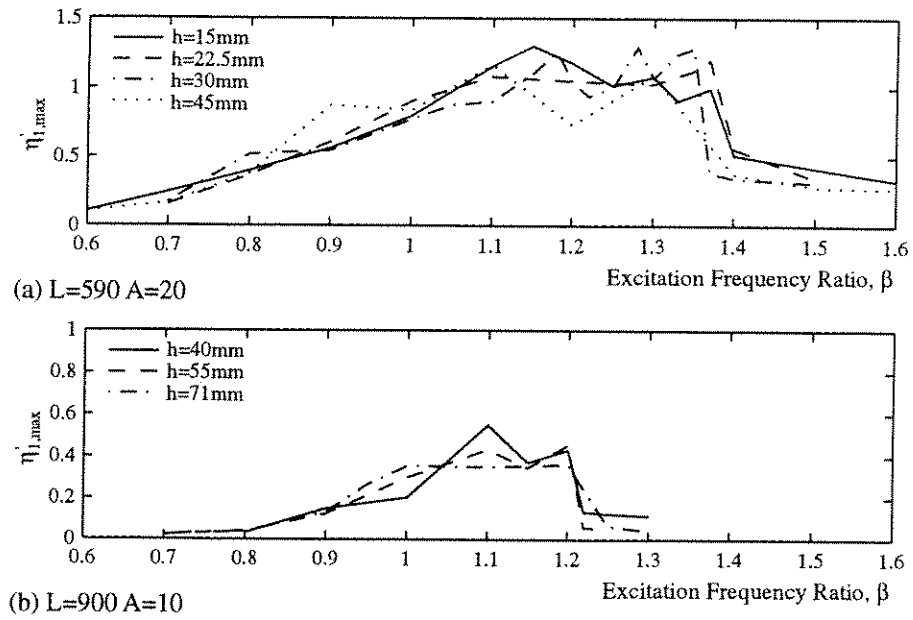


Figure 2.8 Sample frequency responses for the selected experimental cases to investigate the effect of water depth  $h_0$  on the water sloshing motion.

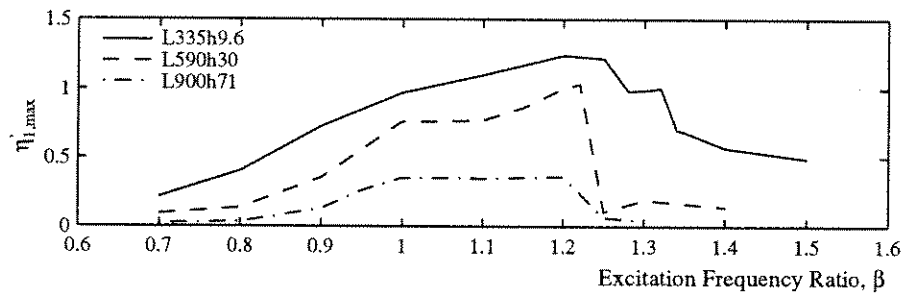


Figure 2.9 Sample frequency responses for the selected experimental cases to investigate the effect of tank length  $L$  on the water sloshing motion.

Based on the shallow-water wave theory, the propagation speed,  $S$ , of a smooth wave may be expressed as

$$S = \sqrt{g(h_0 + \eta)} = \sqrt{gh_0(1 + \eta')} \quad (2.9)$$

where  $\eta' = \frac{\eta}{h_0}$ . Because the wave length  $L_0$  of the fundamental mode of sloshing motion in a rigid tank with length  $L$  can be calculated by  $L_0 = 2L$ , the fundamental frequency of the tank,  $f$ , is calculated by

$$f = \frac{S}{2L} = \frac{\sqrt{gh_0}}{2L} \sqrt{1 + \eta'} \quad (2.10)$$

Considering the “linear” fundamental natural frequency of the shallow-water wave based on Equation (2.1) as

$$f_w \equiv \frac{\sqrt{gh_0}}{2L} \quad (2.11)$$

the ratio of the real fundamental natural frequency to the linear fundamental natural frequency is approximated by

$$\frac{f}{f_w} \equiv \sqrt{1 + \eta'} \quad (2.12)$$

Equation (2.12) indicates that the natural frequency of the shallow-water wave is a function of the wave height. Because the wave height is related to the excitation amplitude  $A$  and the tank length  $L$  as observed in Figures 2.7 through 2.9, the frequency shift ratio is dependent on these two parameters. In other words, the nonlinearity of the shallow-water sloshing is, at least, a function of  $A$  and  $L$ .

As mentioned previously, the jump frequency can be used as a representation of the nonlinearity of the water sloshing motion. Figure 2.10 shows the relationship between the jump frequency and the two parameters  $A$  and  $L$ . In this plot, the parameter “nondimensional excitation amplitude” is introduced, which combines the two parameters in the form of

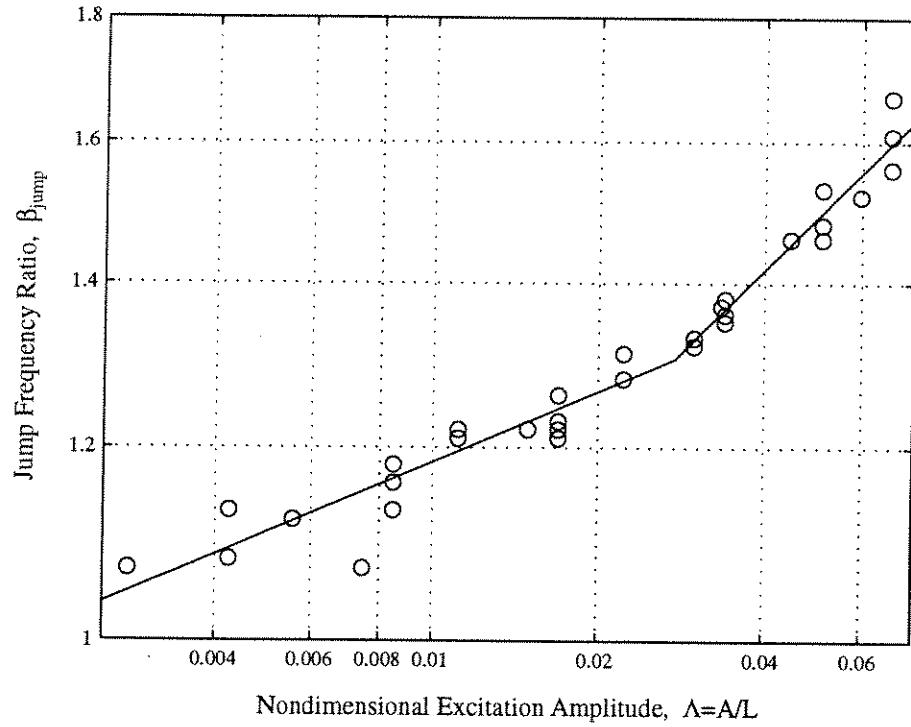


Figure 2.10 Relationship between the jump frequency ratio and the nondimensional excitation amplitude based on experimental results.

$$\Lambda = \frac{A}{L} . \quad (2.13)$$

The values of the jump frequency ratio  $\beta_{jump}$  for all experimental cases described in Table 2.1 were plotted against the nondimensional excitation amplitude. These two parameters exhibit clear correlation. The approximate functional relationship between these two parameters change slope at  $\Lambda \approx 0.03$  in this log-log scale plot. The regression line of  $\beta_{jump}$  on  $\Lambda$  in each region is determined using the least squares method as

$$\begin{aligned} \beta_{jump} &= 1.85\Lambda^{0.095} & \text{as } \Lambda \leq 0.03 \text{ and} \\ \beta_{jump} &= 2.89\Lambda^{0.222} & \text{as } \Lambda \geq 0.03 . \end{aligned} \quad (2.12)$$

These equations reflect that in the region of larger excitation amplitude, approximately  $\Lambda > 0.03$ , the slope of the regression line increases. This means that the rate of change in the jump frequency becomes faster in this excitation amplitude range. This result implies that the nonlinearity of the water sloshing motion changes more rapidly in this region.

### 2.2.3 Higher modes of water sloshing motion

As discussed in the previous section, the higher modes of water sloshing are apparent in the time history responses of the wave height and the base shear force near the resonance frequency. The effects of the higher modes of the water sloshing motion on the energy dissipation plots have been also discussed. In this section, the effects of the higher modes are systematically investigated using the frequency response plots of the experimental results.

Figure 2.11 presents the results of the experimental investigation for the tank with length  $L=590$  mm, water depth  $h_0 = 30$  mm and excitation amplitude  $A = 20$  mm. It contains the plots of  $\eta'_{\max}$ ,  $F'_{w,\max}$ ,  $F'_{w,rms}$  and  $E'_d$  filtered with four different cut-off frequencies such that each curve includes only the low frequency components up to the designated mode. By comparing these curves, the effects of the higher frequency components upon the water sloshing motions are summarized as follows:

- The effect gradually increases as the excitation frequency increases up to jump frequency.
- The effect is most significantly related to  $\eta'_{\max}$ . It is less significantly related to  $F'_w$  and negligible for  $E'_d$ .
- The effect is less for RMS values than peak values of  $\eta$  and  $F_w$ .
- The contribution of the frequency components higher than 9<sup>th</sup> mode on the wave motion is not significant and can be ignored.

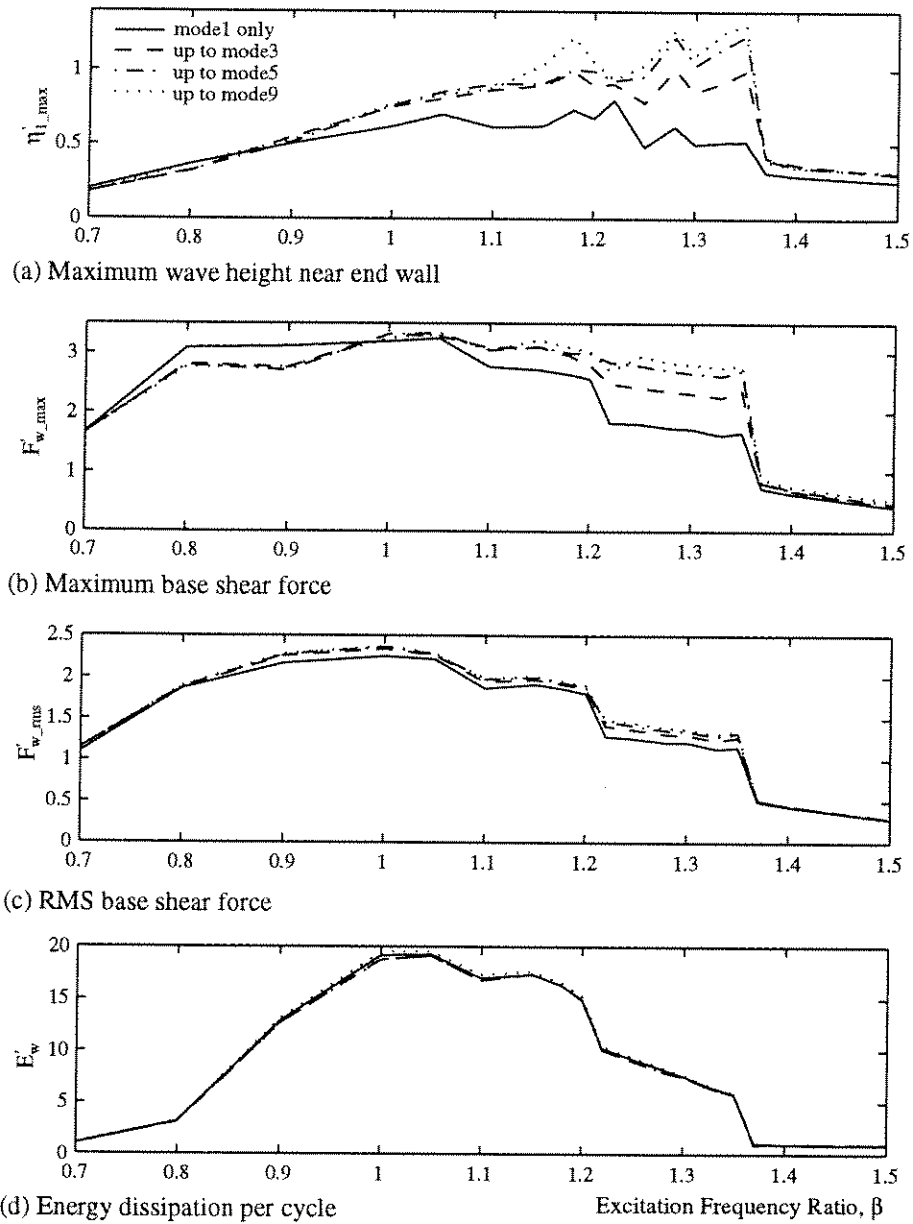


Figure 2.11 The effects of higher frequency components of the water sloshing motion upon its frequency responses for the tank with length  $L = 590$  mm, water depth  $h_0 = 30$  mm and excitation amplitude  $A = 20$  mm.

- The higher frequency components of the water sloshing motion do not contribute to the energy dissipation capacity of the TLD. Therefore, performance of the TLD can be accurately predicted by considering only the fundamental mode of the water sloshing motion.

#### 2.2.4 Calculation of the base shear force based on the wave height near the end walls of rectangular tank.

The TLD generates a hydrodynamic force due to the water sloshing motion. For small amplitude excitation, it is common practice to approximate the hydrodynamic force by the hydrostatic pressures on the tank end walls. In large amplitude excitation, the wave breaks in a certain frequency region. The approximations for hydrostatic pressure and ignoring the vertical acceleration of the water particles must be investigated.

As shown in Figure 2.11, the true water sloshing responses can be closely represented by including low frequency components up to 9<sup>th</sup> mode. Because the 9<sup>th</sup> mode frequencies of the tanks for all experimental cases are lower than 10 Hz at which the system noises exist, the low pass filter with cut-off frequency between the 9<sup>th</sup> mode frequency and 10 Hz was applied to the experimental raw data to eliminate the system noise.

Assuming hydrostatic pressure on the tank end walls and ignoring the vertical acceleration of the water particles, the hydrodynamic force of the TLD,  $F_{\eta}$ , hereinafter the linear hydrodynamic force, can be calculated by

$$F_{\eta} = \frac{1}{2} \rho g b (h_l^2 - h_r^2) \quad (2.15)$$

where  $\rho$  is the water density;  $g$  is the acceleration due to gravity;  $b$  is the tank width and  $h_l$  and  $h_r$  are the water surface elevations at the end walls.

Figure 2.12 presents the frequency responses of the tank with length  $L=590$  mm, water depth  $h_0=30$  mm and excitation amplitude  $A=20$  mm. The solid curves represent the

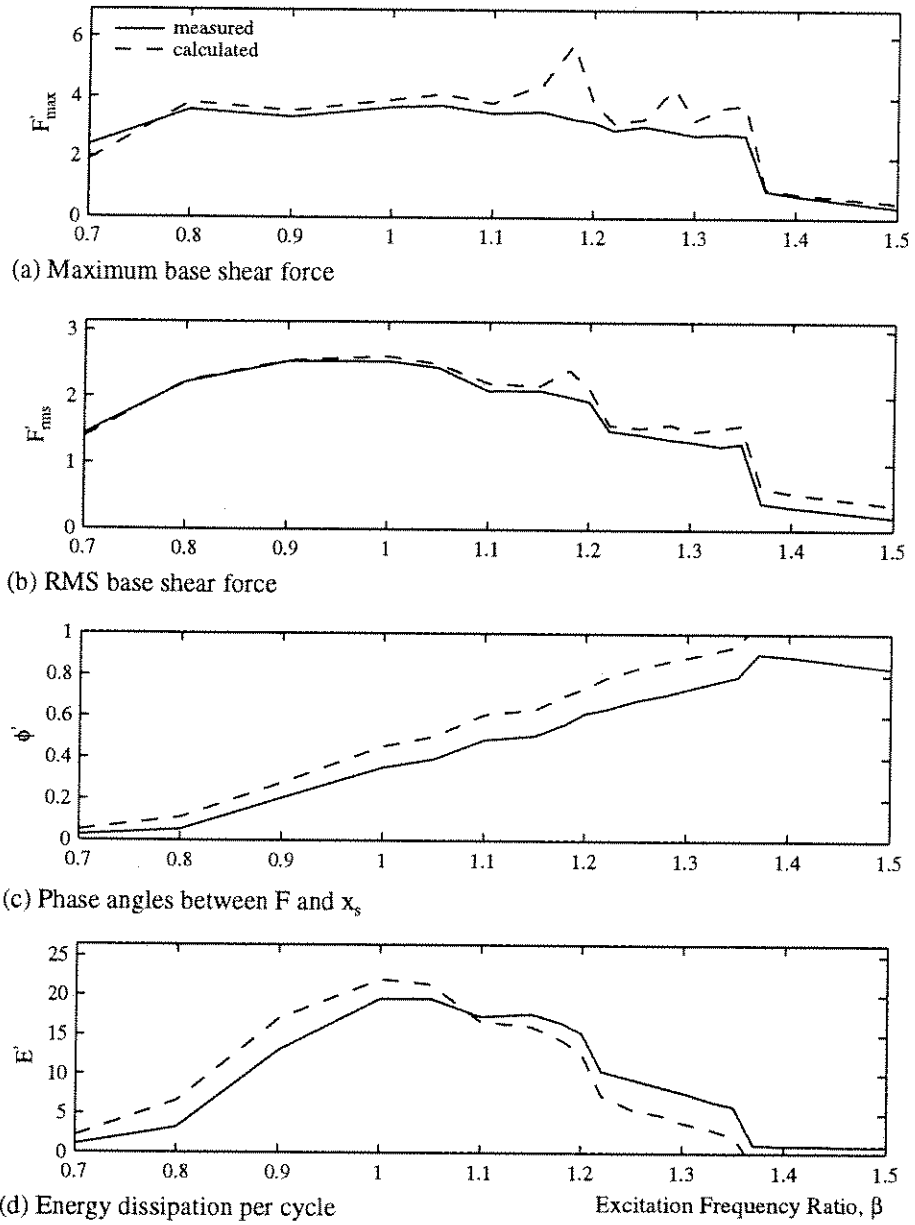


Figure 2.12 Comparison of the base shear force,  $F_{\eta}$ , calculated from the wave height and the one measured by the load cell,  $F_w$  for the tank with length  $L=590\text{mm}$ , water depth  $h_0=30\text{mm}$  and excitation amplitude  $A=20\text{mm}$ .

base shear force,  $F_w$ , measured by the loadcell. The dashed curves indicate the linear hydrodynamic forces,  $F_\eta$ , calculated from the measured wave heights at the end wall of the tank using Equation (2.15). Both data were filtered to retain the lower frequency components up to the 9<sup>th</sup> mode. The nondimensional values of the maximum and RMS base shear forces, the phase angle of the two forces from the shaking table displacement and the energy dissipation per cycle by the two forces are plotted vs. sweep frequency.

In the plot for the maximum values of the two forces, significant discrepancies are observed in both shape and magnitude, particularly near the resonance frequency. These discrepancies can be explained as follows: After the peak wave hits the end wall, the remaining bulk mass of the water runs up the end wall. Although this latter run-up does not develop significant hydraulic pressure, the calculated force derived from wave height alone reaches its maximum value. Consequently, the maximum calculated force may be exaggerated. Because the duration of the wave run-up is short, the discrepancy is reduced in the plots for the RMS of the forces. Plots for the RMS values of two forces are more similar. However, the discrepancy in the magnitude of the damping forces near the resonance frequency is still about 10 to 20 %.

The phase angles of  $F_\eta$  lag behind those of  $F_w$  over the entire range of sweep frequencies. The differences fall within the range of less than  $0.15\pi$ . This discrepancy is assumed to reflect that the maximum value of  $F_\eta$  is captured after maximum  $F_w$  was measured because of the run-up discussed previously and the distance of the wave gage from the end wall. The energy dissipation plots reflect the combined effects of the magnitudes and the phase angles of the two forces.

### 2.3 Water sloshing motion in circular tanks.

The shaking table experiments were conducted for a circular tank with diameter  $D$  of 690 mm. The experimental cases are described on Table 2.2. The experimental cases for the circular tank were selected to maintain the same fundamental natural frequency as the rectangular tank with length  $L=590$  mm and the same water depth.

Figure 2.13 presents sample time history responses of the water sloshing motions at steady-state of the tank with diameter  $D=690$  mm, water depth  $h_0=30$  mm and excitation amplitude  $A=20$  mm at various base excitation frequencies. The measured quantities are the same as for the corresponding rectangular tank cases (Figure 2.3) except  $\eta'_3$  is the nondimensional wave height at the middle of the side wall. It is apparent that the water sloshing motion depends on the excitation amplitude and frequency.

Figure 2.14 shows the frequency responses of the water sloshing motions in the circular tanks for the same cases under the base excitation amplitude  $A = 10, 20$  and  $40$  mm. These cases correspond to the rectangular tank cases presented in Figure 2.7. It is observed that the shapes and the magnitudes of the wave heights, the base shear forces and the energy dissipation per cycle for the circular TLD are similar to those of the corresponding rectangular TLD.

Although the wave behavior in a circular tank is more complex than in the rectangular one, in practice, it is often analyzed as an equivalent rectangular tank. The observation of the similarity in trends of the water sloshing motion in a circular tank and those in the comparable rectangular tank justifies the use of this approximation method for the circular TLD.

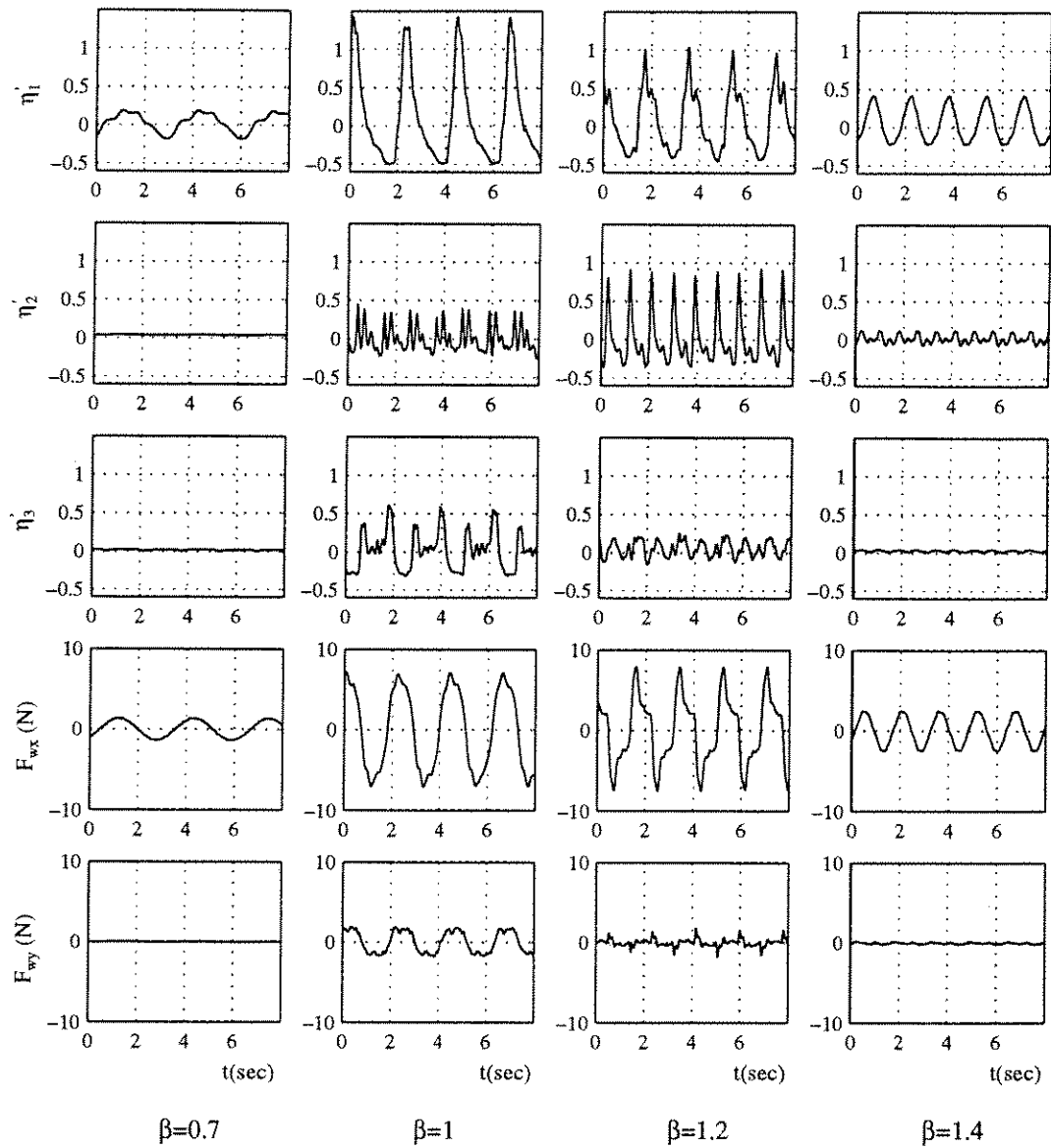


Figure 2.13 Sample time history responses of water sloshing motion for the circular tank with diameter  $D=690\text{mm}$ , water depth  $h_0=30\text{mm}$  and excitation amplitude  $A=20\text{mm}$ .

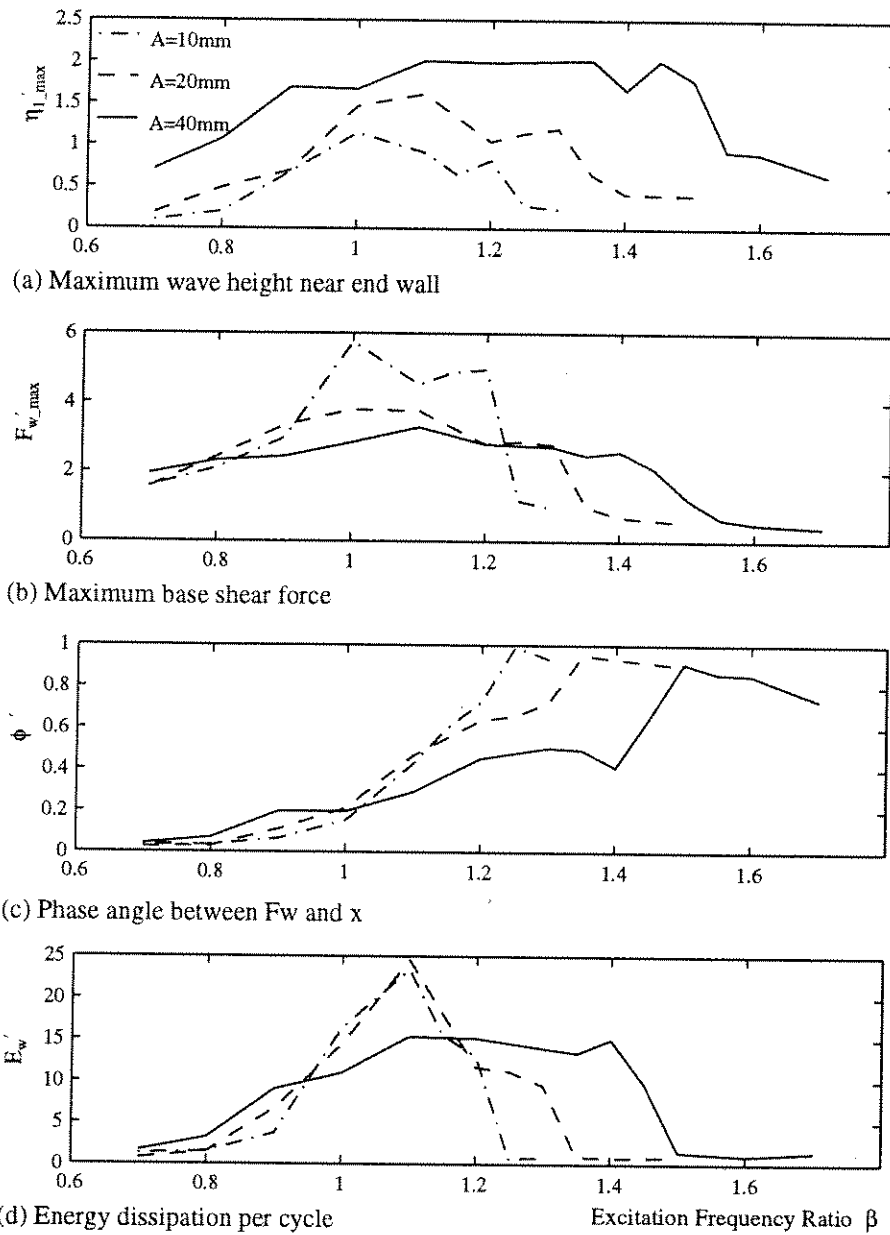


Figure 2.14 Sample frequency responses of water sloshing motion for the circular tank with diameter  $D=690\text{mm}$ , water depth  $h_0=30\text{mm}$  and excitation amplitude  $A=20\text{mm}$ .

## CHAPTER 3

### NUMERICAL MODELS OF THE TLD

Two numerical models were investigated. The first is an equivalent TMD model developed based on the experimental results. This model incorporates the nonlinear stiffness and damping characteristics of the TLD, and is called the “NSD model”.

The second model is a fluid model based on the shallow-water wave equations characterized using the random choice method (RCM model) which was proposed by Gardarsson and Yeh (1994). A series of numerical analyses were conducted using this model to simulate the water sloshing motion in rectangular tanks. This model is evaluated by comparing the results with the experimental investigations.

#### **3.1 NSD model - an empirically-based equivalent TMD model**

The behavior of passive TMDs has been thoroughly investigated, e.g., McNamara (1977); Warburton (1980, 1981, 1982). The use of a TMD model to represent the TLD is attractive because of the body of knowledge devoted to the TMD and the similarity in the mechanisms of the TLD and TMD as described in Section 1.2. In this investigation, an equivalent TMD model that incorporates the nonlinear stiffness and damping characteristics is developed on the basis of experimental results. This model is called the “NSD model”.

##### **3.1.1 Modeling**

As discussed in Section 1.2, the water mass of the TLD reacts to the structural movement in a similar manner as the mass of the TMD. The TLD exhibits its inherent damping and stiffness characteristics due to its sloshing motion. After the damping and stiffness of the TLD are quantified, the TLD can be modeled as a SDOF mass with stiffness and damping.

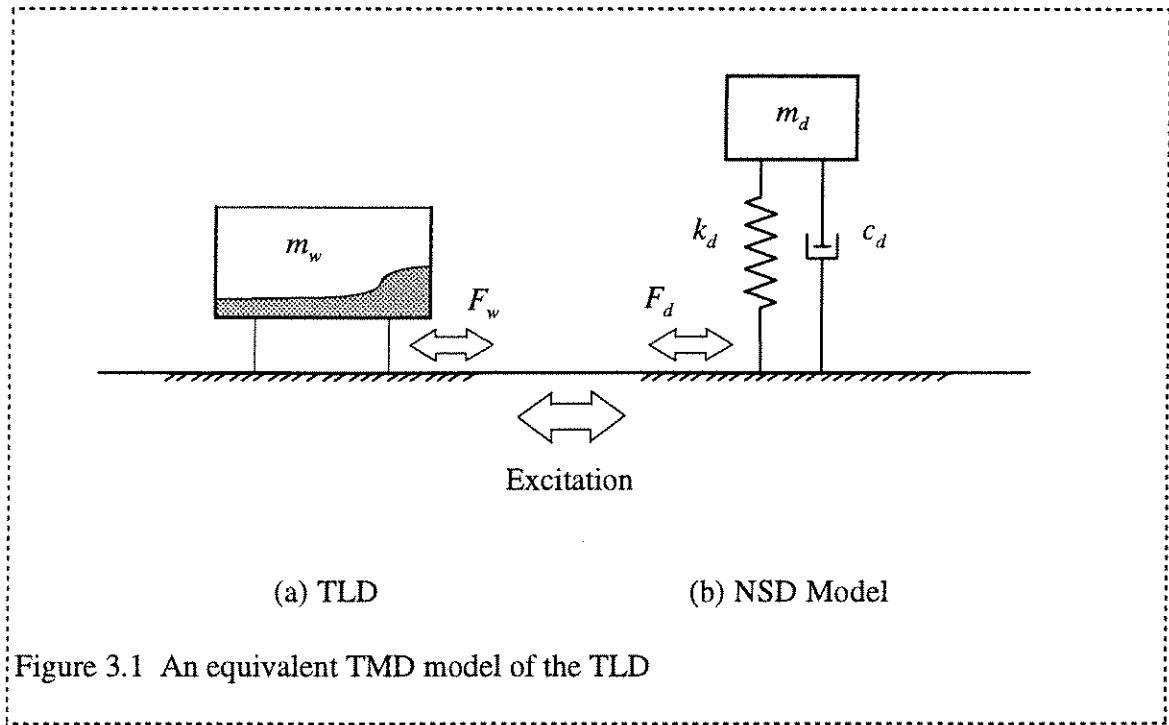


Figure 3.1 illustrates a TLD and the proposed equivalent TMD model as a SDOF system with stiffness and damping parameters,  $k_d$  and  $c_d$ , respectively. However, unlike the TMD which is considered as a linear system, the TLD possesses strong nonlinear characteristics as observed in the shaking table experiments and must be modeled as a nonlinear system. The stiffness and damping of the NSD model are determined such that the base shear force (or damping force) due to the TLD,  $F_w$ , and that due to the corresponding NSD model,  $F_d$ , are equivalent under the same base excitation.

The damping force is characterized by its amplitude and phase. Alternatively, the single parameter of energy dissipation per cycle,  $E_d$ , can be used to match the properties of a TLD with its equivalent TMD representation. The energy dissipation per cycle is defined by the area inside the loop of the damping force vs. the base displacement contour as described by Equation (2.5). This quantity represents the combined effects of the amplitude and the phase of the damping force on the structural motion over the period of

one cycle.<sup>1</sup> In determining the properties of the NSD model, a comparison of the energy dissipation has advantages over a comparison of the damping forces of two systems. First, comparing one scalar quantity is more appealing. Second, as illustrated in Figure 2.11, the effect of higher modes of the water sloshing on the quantity of the energy dissipation is negligible. Therefore, in this investigation, the energy dissipation is employed as a parameter for determining model parameters.

### 3.1.2 Energy dissipation matching scheme

Figure 3.2 presents typical sweep frequency plots of the nondimensional energy dissipation per cycle for the TLD with length  $L = 590$  mm, water depth  $h_0 = 30$  mm and excitation amplitude  $A = 20$  mm and for its corresponding NSD model. The nondimensional energy dissipation curve for the TLD ( $E_w'$ , solid line) is determined from measurements of the shaking table experiments using Equations (2.5) and (2.6). The nondimensional energy dissipation for the corresponding NSD model ( $E_d'$ , dashed line) is calculated using the procedure described in Appendix A.2 and summarized here. In presenting this procedure, the following parameters are used:  $f_e$  indicates the excitation frequency;  $f_w$  represents the linear fundamental natural frequency of the TLD as defined in Equation (2.1);  $\omega_w$  is the linear fundamental natural angular frequency of the TLD defined by  $\omega_w = 2\pi f_w$ ;  $\beta$  is the excitation frequency ratio as defined in Equation (2.8);  $m_w$  is the mass of the water in the tank;  $k_w$  is the linear fundamental stiffness of the TLD defined by  $k_w = m_w \omega_w^2$ ;  $m_d$ ,  $k_d$  and  $c_d$  are the mass, stiffness coefficient and damping coefficient of the corresponding NSD model, respectively; the critical damping ratio is defined as  $c_{cr} = 2m_w \omega_w$ ; and the damping ratio of the equivalent TMD model,  $\zeta$ , is defined by

$$\zeta = \frac{c_d}{c_{cr}} . \quad (3.1)$$

<sup>1</sup> See Appendix A.2 for the relationship of energy dissipation to the damping force in SDOF system.

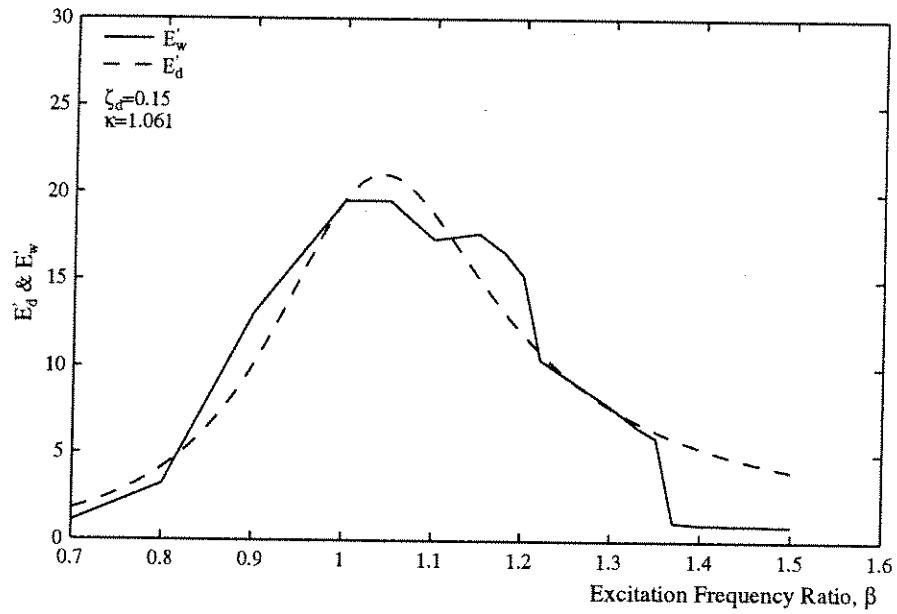


Figure 3.2 Matching scheme of the sweep frequency energy dissipation curves to obtain the stiffness hardening ratio,  $\kappa$ , and damping ratio,  $\zeta_d$ , of the NSD model of the TLD with length  $L=590\text{mm}$ , water depth  $h_0=30\text{mm}$  and excitation amplitude  $A=20\text{mm}$ .

The stiffness hardening ratio,  $\kappa$ , is defined by

$$\kappa = \frac{k_d}{k_w} . \quad (3.2)$$

The frequency shifting ratio,  $\xi$ , is defined by

$$\xi = \frac{f_d}{f_w} . \quad (3.3)$$

If the NSD model shown on Figure 3.1 (b) is subjected to a harmonic base excitation with frequency ratio  $\beta$ , the amplitude and the phase of the damping force are expressed respectively, in nondimensional form as follows<sup>1</sup>

<sup>1</sup> See Equations (A.16) & (A.7) in Appendix A.

$$|F_d'| = \frac{\sqrt{(1 + (4\zeta^2 - 1)\beta^2)^2 + 4\zeta^2\beta^6}}{1 + (4\zeta^2 - 2)\beta^2 + \beta^4} \quad (3.4)$$

$$\text{and} \quad \phi = \tan^{-1} \left( \frac{2\zeta\beta^3}{-1 + (1 - 4\zeta^2)\beta^2} \right). \quad (3.5)$$

The nondimensional energy dissipation for the NSD model at each excitation frequency is obtained by the formula<sup>1</sup>

$$E_d' = 2\pi |F_d'| \sin \phi. \quad (3.6)$$

$E_d'$  is fit to  $E_w'$  by the least squares method over the frequency range of high energy dissipation. In general, this matching region encompasses approximately 70 % of the peak energy dissipation. The fundamental trends of the  $E_d'$  curve for various model parameters are described in Appendix A.2.

### 3.1.3 Determination of the model parameters based on shaking table test results for rectangular TLDs

The matching scheme discussed in the previous section was applied to the experimental cases for rectangular TLDs to determine the stiffness and the damping coefficients of the equivalent TMD model. In general, for the case with smaller excitation amplitude, the  $E_w'$  curve becomes higher and narrower, which corresponds to lower damping and lower stiffness of the model. As the excitation amplitude becomes larger, the response curve becomes lower and wider, which leads, consequently, to higher damping and higher stiffness of the model. The specific results are tabulated in Table E.1 in Appendix E.

As discussed in Section 2.2 and illustrated in Figure 2.10, the nonlinearity of the TLD in terms of jump frequency can be expressed as a function of  $A$  and  $L$ . Sun, et al.

---

<sup>1</sup> See Equation (A.19) in Appendix A.

(1992) found that the nonlinearity of the TLD also depends on the parameter  $\varepsilon$  that is the ratio of water depth  $h_0$  to the tank length  $L$ . The damping of the shallow water sloshing motion is difficult to determine analytically, especially, for wave breaking situations. However, the damping ratio of rectangular TLD under small excitation amplitude is expressed in Sun (1992) as

$$\zeta_w = \frac{\sqrt{\omega\nu}(1 + 2h_0/B + S)}{2\sqrt{2}(\eta + h_0)\omega_w} \quad (3.7)$$

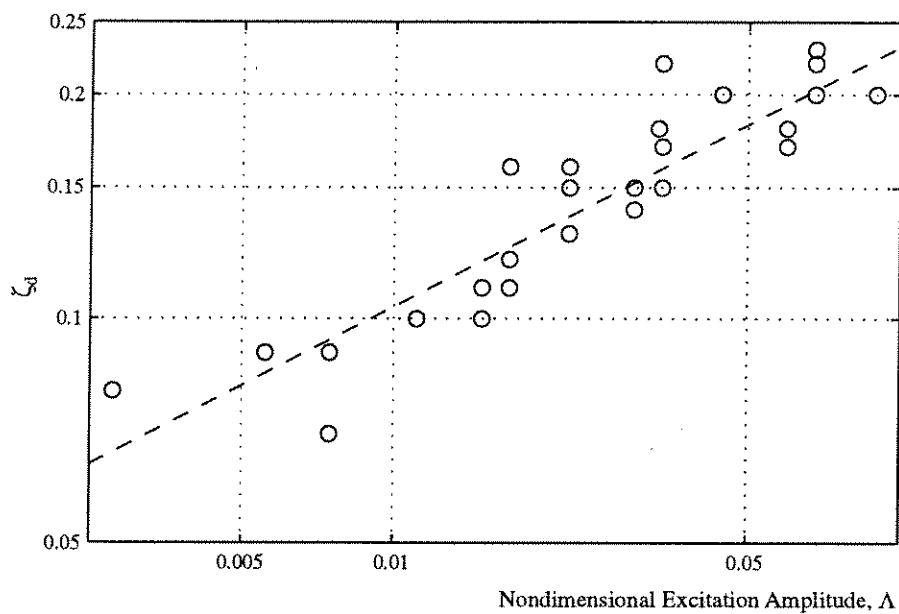
which is a function of  $h_0$ . Therefore, it was assumed that the stiffness and the damping coefficients are functions of three parameters:  $A$ ,  $L$  and  $h_0$ . To determine the contribution of each parameter to the nonlinearity of the TLD, the two coefficients were plotted against various combinations of these three parameters. The combination of three parameters with which the data are best correlated is the best parameter for representing the nonlinearity of the TLD. The nondimensional excitation amplitude for both coefficients ( $\zeta$  and  $\kappa$ ) was determined through an extensive searching for the best correlation as

$$\Lambda = \frac{A}{L} . \quad (3.8)$$

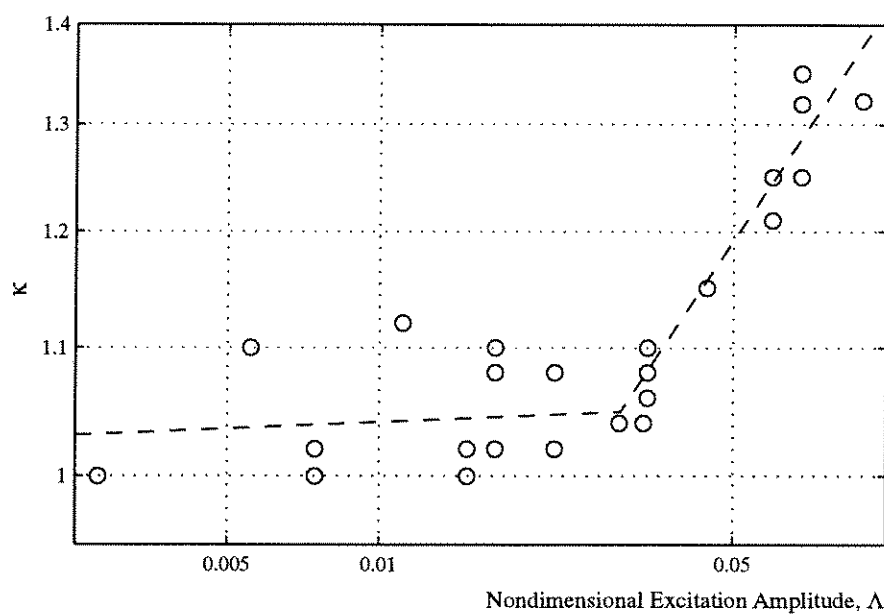
This is the same parameter for the jump frequency plot as shown in Equation (2.13).

In Figure 3.3, the variation of damping and stiffness hardening ratios of the equivalent TMD models for the experimental cases is plotted with respect to the nondimensional excitation amplitude,  $\Lambda$ . The damping ratios are clearly correlated with  $\Lambda$  over the entire range of excitation amplitude. The best fitted curve was determined using the least squares method as

$$\zeta_d = 0.52\Lambda^{0.35} . \quad (3.9)$$



(a) Damping ratio



(b) Stiffness hardening ratio

Figure 3.3 The damping ratio,  $\zeta_d$ , and the stiffness hardening ratio,  $\kappa$ , of the NSD model of the rectangular TLD determined from shaking table experiment.

For the stiffness hardening ratio of the NSD model, the figure shows two distinct regions divided at  $\Lambda \approx 0.03$ . In each region the slope is clearly different. This phenomenon is consistent with the observation from the jump frequency plots. The two regions are defined as the weak wave breaking region and the strong wave breaking region, respectively. The regression line in each region was determined using the least squares method as

$$\begin{aligned} \kappa &= 1.075\Lambda^{0.007} & \text{as } \Lambda \leq 0.03 & \text{ and} \\ \kappa &= 2.52\Lambda^{0.25} & \text{as } \Lambda > 0.03. \end{aligned} \quad (3.10)$$

In the weak wave breaking region, the stiffness hardening ratio changes very slowly at the approximate value of 1.05. The stiffness hardening ratio changes rapidly in the strong wave breaking region. Noticing the relationship between  $\xi$  and  $\kappa$  as

$$\xi = \sqrt{\kappa}, \quad (3.11)$$

the frequency shift ratio may be expressed as

$$\begin{aligned} \xi &= 1.038\Lambda^{0.0034} & \text{as } \Lambda \leq 0.03 & \text{ and} \\ \xi &= 1.59\Lambda^{0.125} & \text{as } \Lambda > 0.03. \end{aligned} \quad (3.12)$$

### 3.1.4 Application of the equivalent TMD model derived for rectangular TLDs to the circular TLD

Because a structure moves in many directions, the circular shape TLD may have advantages in mitigating vibration over the rectangular one. However, wave motions in the circular tank are more complex than those in the rectangular one. In practice, therefore, the circular TLD is often analyzed as an equivalent rectangular TLD, e.g., Wakahara (1993). The conversion of a circular TLD into rectangular one is made such that the fundamental natural frequency and the mass of two TLDs with the same water depth are equal. To maintain same natural frequencies of the two system, Equations (2.1) and (2.2) are set equal. The length of the equivalent rectangular TLD,  $L$ , is obtained in terms of the diameter of the circular TLD,  $D$ , as

$$L = 1.17D . \quad (3.13)$$

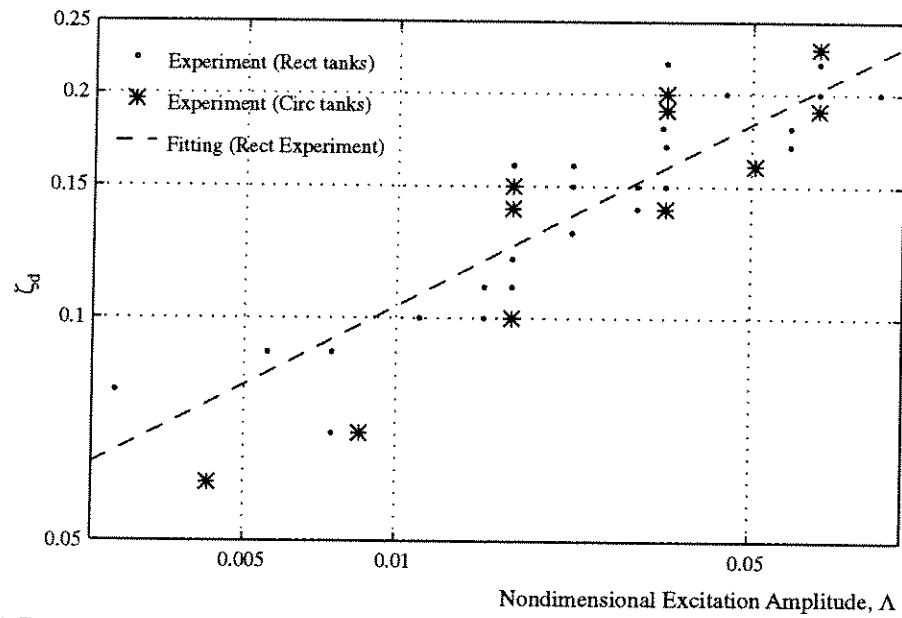
To maintain equal masses of the two systems, the width of the rectangular tank,  $B$ , is obtained by

$$B = 1.075 L . \quad (3.14)$$

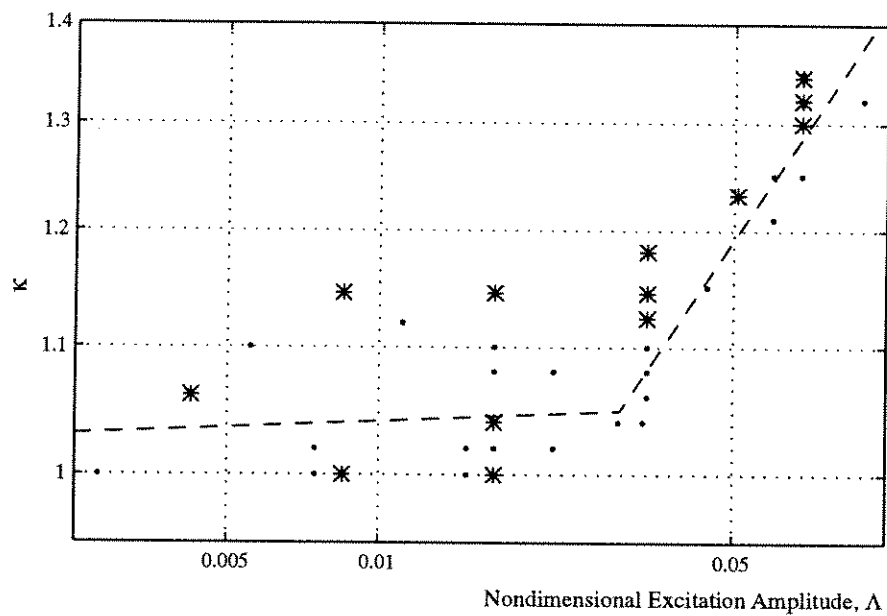
The matching procedures were applied to the energy dissipation curves obtained from the shaking table experiments for the circular tank with diameter  $D = 690$  mm and various water depths. The damping ratios and the stiffness hardening ratios for each circular tank are tabulated in Table E.3 in Appendix E and plotted in Figure 3.4. From Equation (3.13) the length of the equivalent rectangular tank is found to be  $L = 590$  mm. For comparison purposes, the results for rectangular tanks and its best fitted curves are plotted in the same figure.

In the region of weak wave breaking, i.e.,  $\Lambda < 0.03$ , the data points are scattered from the fitted curve in the plot of stiffness hardening ratio. This discrepancy appears to reflect the phenomenon of swirling wave motion in the circular tank near the resonance excitation frequency. The swirling wave motion reduces the energy dissipation capacity.

However, overall, the NSD properties of the circular TLD are similar to those of the equivalent rectangular TLD. The result justifies the method of analysis of the circular TLD as an equivalent rectangular one.



(a) Damping ratio



(b) Stiffness hardening ratio

Figure 3.4 The damping ratio,  $\zeta_d$ , and the stiffness hardening ratio,  $\kappa$ , of the NSD model of the circular TLD determined from shaking table experiment.

### 3.2 RCM model - a numerical fluid model

The water sloshing motions were simulated numerically using the random choice method (RCM) that was proposed by Gardarsson and Yeh (1994). The shallow-water wave theory is briefly discussed prior to introducing the RCM model. The results of numerical analyses using the RCM model are presented and compared with the experimental data.

#### 3.2.1 Shallow-water wave theory

In this section, background information on shallow-water wave theory is briefly described; the details are presented in Appendix F.

The shallow-water wave theory is based on the depth-averaged equations of mass and momentum conservation. The derivation of these equations involves the assumptions that water is an incompressible and inviscid fluid, the water depth is infinitesimally small in comparison with the characteristic horizontal length scale of the motion, the pressure field is hydrostatic everywhere, and the horizontal velocity is uniform throughout the depth. If one dimensional wave propagation is considered, the shallow-water equations of mass and momentum conservation are respectively,

$$h_t + (uh)_x = 0 \quad (3.15)$$

and 
$$u_t + uu_x + gh_x = 0 \quad (3.16)$$

where all parameters are defined in Figure F.1 in Appendix F.

Free-surface flows like sloshing motion in a tuned liquid damper cannot create a significant pressure difference in the field so that the effect of water compressibility is considered to be negligible. While the energy dissipation associated with turbulence can be important, direct viscous effect on the fluid motion is negligible for the high Reynolds number flows typical of those in a tuned liquid damper. For the TLD, the water depth is usually much smaller than the horizontal dimension of the tank, which implies that the assumptions of the infinitesimal flow depth and hydrostatic pressure field are justified.

A wave described by the shallow-water wave equations propagates with a speed independent of its wave length, but dependent on its amplitude: the higher the wave amplitude, the faster it propagates. In other words, the shallow-water wave theory represents a non-dispersive and fully nonlinear wave system. The models based on the non-dispersive, fully-nonlinear shallow-water wave equations are believed capable of modeling wave-breaking, including the effect of energy dissipation, although the breaking is not characterized in detail but as a flow-property discontinuity. In fact, it is this property for which the shallow-water wave theory was adopted to analyze the sloshing motion in a tuned liquid damper since the focus is on the response under large amplitude excitation.

### 3.2.2 Numerical simulation of water sloshing motion using the RCM model

A numerical scheme to solve the shallow-water wave equations using the random choice method (RCM model) was proposed by Gardarsson and Yeh (1994). The random choice method is a shock-preserving scheme; the shock is represented by the discontinuities of water surface elevation and velocity between two adjacent grid points. This scheme causes no numerical dissipation or dispersion and follows precisely the mathematical formulation of the shallow-water wave theory. However, it has limitations in simulating the real fluid sloshing motion. For example, in a real fluid environment, the breaking wave front is not a discontinuity and the pressure field is not exactly hydrostatic, especially near the breaking wave front.

A series of numerical simulations as described in Table E.2 in Appendix E.2 were undertaken using the RCM model. The length of the tank was meshed with 400 grid points. In order to obtain the steady state responses, each case was run for 80 cycles of the linear fundamental natural period of the tank,  $T = 1/f_w$  where  $f_w$  is the linear fundamental natural frequency of the tank which is calculated using Equation (2.31). As discussed in Section 2.2.4, the hydrodynamic forces of the TLD were calculated based on the hydrostatic pressures on the tank end walls using Equation (2.7).

Figure 3.5 shows the time history responses of the water sloshing for the case of  $L=590$  mm,  $h_0=30$  mm and  $A=20$  mm. A comparison of these numerical results with the experimental ones presented in Figures 2.4 thru Figure 2.6 reveals discrepancies. It appears that the numerical scheme cannot simulate the higher frequency components observed in the experimental investigations in a satisfactory manner. However, the overall shapes of the time history responses are in good agreement with the ones obtained from the experimental investigations.

Figure 3.6 presents the frequency responses of the water sloshing for the same case. Several discrepancies are observed in comparing the results from the numerical simulations with the experimental investigations. One apparent difference is that the numerical scheme fails to simulate the jump phenomenon observed in the experimental investigation. The other discrepancies are mostly the result of failure in simulation of the higher modes of the water sloshing motion as discussed in the time history response plots.

The discrepancies are reduced in the plots of RMS base shear force and the energy dissipation per cycle. This observation is consistent with the effects of higher modes on the water sloshing motions discussed in Section 2.2.3. However, considering the difficulties in simulating the wave breaking, the RCM model predicts the water sloshing motion with wave breaking with a satisfactory accuracy, particularly, in terms of the energy dissipation capacity.

As described in Section 3.1.2, the damping and stiffness values of a TLD can be determined using the energy dissipation matching scheme. This procedure was applied to the rectangular TLDs described in Table E.2 of Appendix E. The results are plotted in Figure 3.7 as cross-marks. For comparison purposes, the experimental results (dotted marks) and its best fitted curve (dashed line) are presented also in the figure.

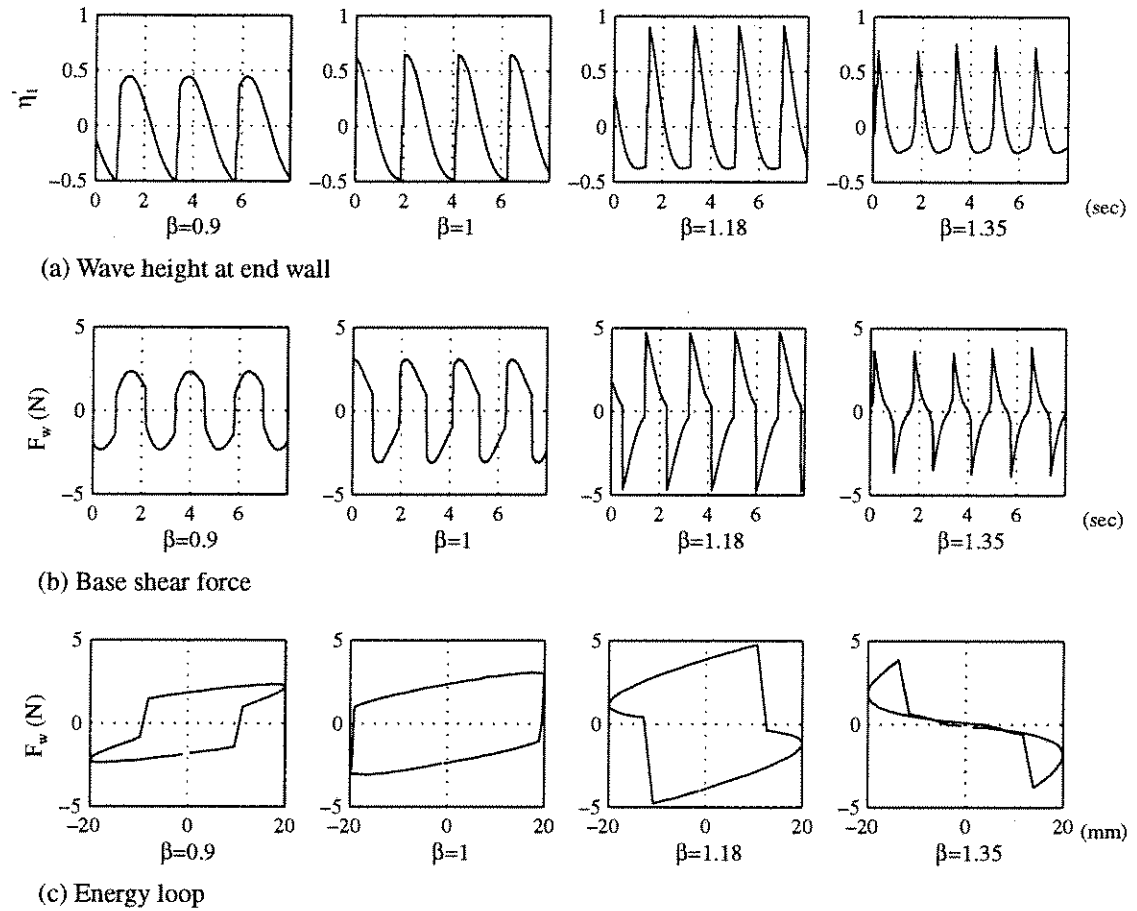


Figure 3.5 Sample time history responses of water sloshing motion simulated using the RCM model for the rectangular tank of  $L=590\text{mm}$ ,  $h_0=30\text{mm}$  and  $A=20\text{mm}$

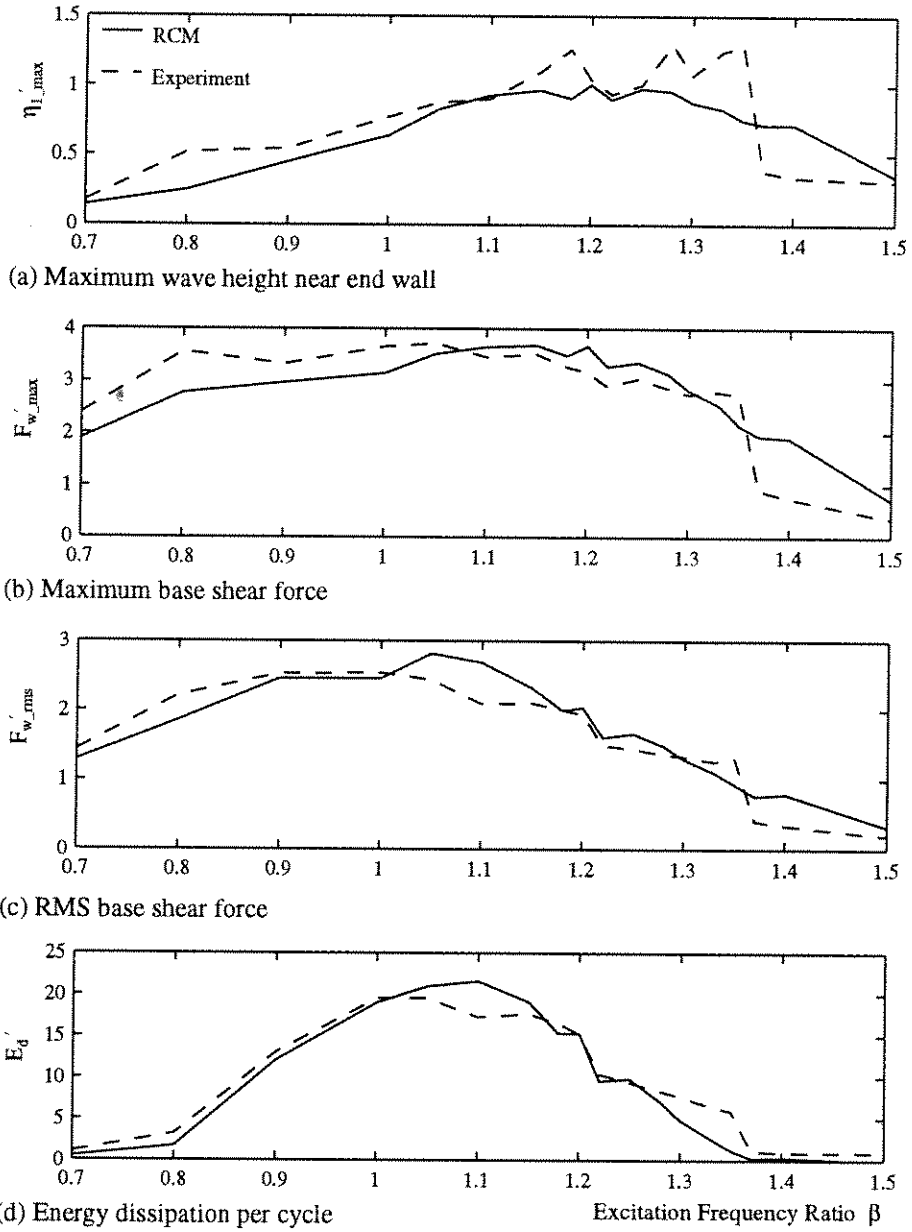
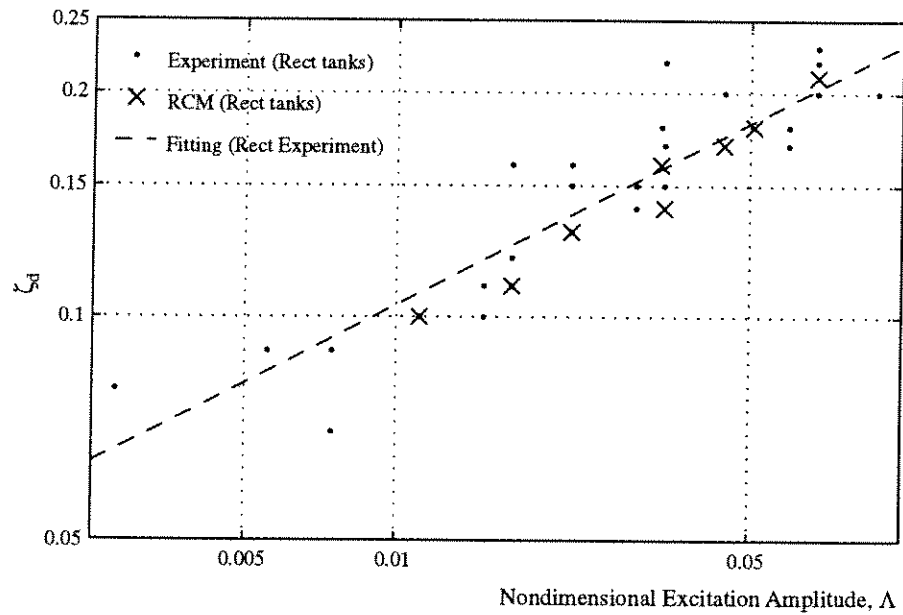
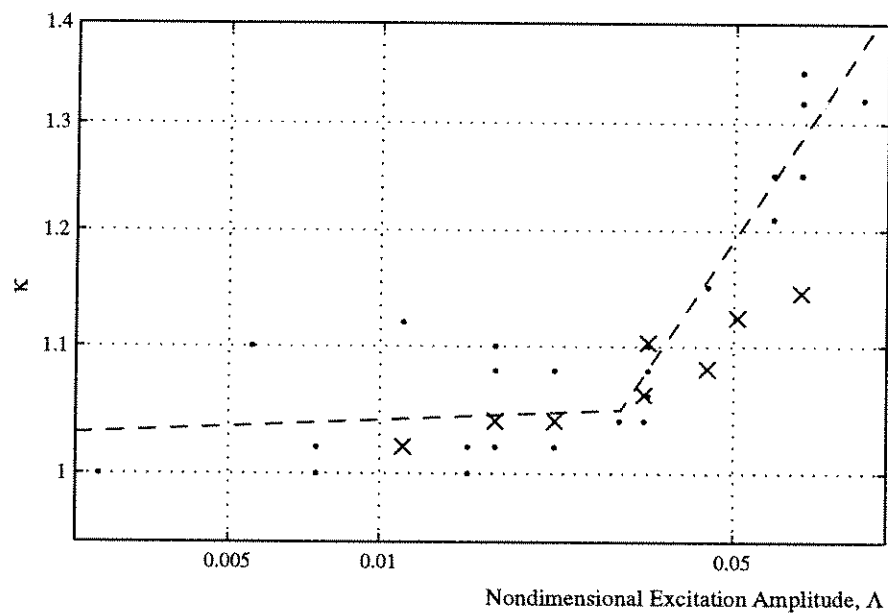


Figure 3.6 Sample frequency responses of water sloshing motion simulated using the RCM model for the rectangular tank of  $L=590\text{mm}$ ,  $h_0=30\text{mm}$  and  $A=20\text{mm}$ .



(a) Damping ratio



(b) Stiffness hardening ratio

Figure 3.7 The damping ratio,  $\zeta_d$ , and the stiffness hardening ratio,  $\kappa$ , of rectangular TLDs determined from numerical analyses using the RCM model.

The results from numerical simulations show good agreement with the experimental results in estimating the damping values of the TLDs in the entire range of excitation amplitudes. Two results also agree well in estimating the stiffness of the TLDs over the range of excitation amplitude  $\Lambda < 0.03$ , i.e., weak wave breaking region. However, in the strong wave breaking region, i.e.,  $\Lambda > 0.03$ , the RCM model under-estimates the stiffness hardening characteristics of the TLD. This result confirms that the RCM model cannot accurately simulate the wave phenomenon under extremely strong excitation motions. It is, however, concluded that the RCM model accurately predicts the water sloshing motion for other breaking wave phenomena.